ORIGINAL RESEARCH

Ultrasonic lateral modulation imaging, speckle reduction, and displacement vector measurements using simple single-beam scanning or plural crossed-beam scanning with new spectra frequency division processing methods

Chikayoshi Sumi
Yousuke Ishii

Department of Information
and Communication Sciences,
Faculty of Science and Technology,
Sophia University, Tokyo, Japan

Correspondence: Chikayoshi Sumi;
Yousuke Ishii
Department of Information and
Communication Sciences, Faculty
of Science and Technology, Sophia
University, 7-1, Kioicho, Chiyoda-ku,
Tokyo, 102-8554 Japan
Tel +81 3 3238 3415
Fax +81 3 3238 3321
Email 8ft2x@symphony.plala.or.jp

Abstract: The development of effective ultrasonic tissue displacement measurement methods increases the number of possible applications for various tissue displacement and strain measurements. These applications include measurements of spontaneous motions/deformations generated by heart motion; pulsations from phenomena such as blood flow (intracardiac, intravascular, and carotid); heart, blood vessel, and liver motion; and motion from artificial sources such as motions/deformations generated by applying static compression/stretching forces, vibration or acoustic radiation forces (breast and liver). For arbitrary orthogonal coordinate systems obtained using arbitrary transducer types (eg, linear, convex, sector, arc, or radial array types, or single aperture types with a mechanical scan), several lateral modulation (LM) methods (eg, scanning with plural crossed or steered beams over a region of interest) have been developed that can be used with new echo imaging methods for tissue displacement/deformation measurements. Specifically, by using such beamforming methods, in addition to highly accurate displacement vector and lateral displacement measurements, LM echo imaging with a high lateral carrier frequency and a high lateral resolution has been developed. Another new beamforming method, referred to as "a steering angle (ASTA) method," ie, scanning with a defined steering angle, is also described. In addition to conventional non-steered-beam scanning (ie, a version of ASTA) and conventional steered-beam scanning with a variable steering angle (eg, sector, arc, radial scan), a simple, single-beam scanning method also permits the use of LM, which yields an accurate displacement vector measurement with fewer calculations than the original LM methods. This is accomplished by using a previously developed spectra frequency division method (SFDM). However, the lateral carrier frequency and the measurement accuracy acquired by using such a single-beam scanning method are lower than those achieved with the original LM scanning methods and should be increased (ie, by using a quasi-LM method). In this report, the effectiveness of the use of the new SFDMs is verified with experiments on agar phantoms, in which conventional non-steered, focused single-beam transmission/reception scanning is performed together with high-speed non-steered single plane-wave transmission and non-steered, focused single-beam reception scanning using a linear array-type transducer. For comparison, the original LMs, with their respective transmissions of crossed, steered focused beams and plane waves are also performed. Because the use of rectangular apodization functions (ie, no apodization) yields a larger bandwidth in a lateral direction than the effective use of parabolic functions with the original LM method, it is shown that disregarding the lateral low-frequency spectra yields useful quasi-LM echo imaging with a high lateral frequency, and

Reports in Medical Imaging 2012:5 57–101

further significantly increases the measurement accuracy of a displacement vector. In addition, when no apodization is used with the original version of LM, disregarding the low-frequency lateral spectra is effective. In addition, the interchangeability of cosine and sine modulations performed after completing beamforming can also be used for single-beam scanning as well as for the original LM scanning method. Specifically, the cosine and sine modulations, respectively, are used for LM and quasi-LM imaging and displacement vector measurements. It is concluded that the appropriate use of the new SFDMs with simple single-beam scanning or with simple plural crossed-beam scanning with no apodization can achieve almost the same accuracy as the original LM scanning method using plural crossed beams with the effective apodization. Another new application of SFDM is also described: an incoherent superposition of the frequency-divided spectra reduces speckles. The new methods will also be effective for other beamforming methods and with other types of transducers.

Keywords: lateral modulation scanning, single-beam scanning, apodization, spectra frequency division method, low-frequency spectra, quasi-LM imaging, coherent superposition, incoherent superposition

Introduction

Various ultrasound (US) displacement/velocity measurement methods have been extensively developed for measurements of blood flow (eg, the continuous-wave Doppler method [DM],[1] the pulse-wave DM,[2] the autocorrelation method [AM],[3] the cross-correlation method [CCM][4]) and tissue strain (eg, DM, AM,[5] and CCM[6]). Methods have also been developed for the analysis of sonar data and for other target motions. For approximately the past 60 years, tissue axial displacement, velocity, and strain have been measured using such methods (ie, one-dimensional [1D] measurement methods), whereas other developments have permitted measurements of multidimensional displacement/velocity vectors, of strain/strain rate tensors for blood flow[7] (intracardiac, intravascular, carotid artery, etc), and for tissue motion (in the liver, etc)[8] (ie, multidimensional CCM).

Sumi et al have also described other displacement measurement methods.[9–19] For instance, the multidimensional cross-spectrum phase gradient method,[9,10] the multidimensional autocorrelation method (MAM),[11–13] and the multidimensional Doppler method (MDM)[11–13] were developed for displacement vector measurements: specifically, for simultaneous axial (or depth), lateral, and elevation displacement measurements. Such methods can be applied to measurements of blood flow and motion/deformation of the heart, blood vessels, liver, skin, muscle, etc, under normal spontaneous motion or artificial motion (static compression/stretching, vibration, acoustical radiation forces, etc).[20,21] The displacement vector, velocity vector, strain tensor, and strain rate tensor are simultaneously measured, and can also be used for estimating the mechanical properties of such tissues,[21] such as shear moduli.

For displacement vector measurements, previously developed lateral modulation (LM) methods[11–19] are effective. These LM methods can be used only through the use of physically superposed, crossed, steered beams.[11–19] Specifically, this includes the use of superposed multiple steered beams with different steering angles either using the multiple transmission method (MTM)[20,22] or those synthesized from a set of received echo data using the multidirectional synthetic aperture method (MDSAM)[20,22] (see figure A1 in Sumi et al[23]). For LM methods, simultaneous or successive transmissions/receptions of US beams can be used. Multiple transducers can also be used. LM permits echo imaging with almost the same lateral resolution as the axial resolution.[15,16] For displacement vector measurements, another LM is performed using the Fraunhofer approximation.[24–27] This common approach uses an apodization function that displays several continuous peaks and performs analog LM processing twice to obtain multidimensional analytic signals. In contrast, the digital LM approach described by Sumi et al produces analytic signals with fewer US transmissions and less processing.[13] Although 1D measurement methods can also be used for LM,[17–19,24–27] MTM,[28,29] and MDSAM,[30] in place of the multidimensional measurement methods,[11–22] decorrelation of local echo signals occurs due to target displacement in a direction orthogonal to the beams. Although a new demodulation method[17–19] was developed for LM that uses only digital signal processing and differs from other demodulation methods,[25,27] the use of 1D measurement methods, even with the multidimensional moving average,[11–13,22] results in a lower measurement accuracy and more processing than the corresponding multidimensional measurement methods.[9,10,13,31,32]

Recently, Sumi et al described a steering angle (ASTA) method,[17,18] a beamforming method that is a simpler than LM, MTM, and MDSAM. ASTA[17,18] uses only a defined steering angle. All of the beamforming methods, including ASTA, can be performed on the same arbitrary orthogonal coordinate systems. Thus, ASTA has several advantages over LM, MTM, and MDSAM,[17,18] and fewer calculations are required to complete beamforming than with LM, MTM, and MDSAM (see Sumi[18] or figure A1 in Sumi et al[23]). Consequently, tissue

motion artifacts, which can occur with LM using plural transmitted beams with a time difference, are not generated. Also, inhomogeneities in tissue properties, such as propagation speed, do not affect focusing (ie, the beam-crossing position) because multiple beams that have different paths are not used. Because only a single quadrant or octant spectra is obtained using ASTA, Sumi et al described a spectra frequency division method (SFDM)[18,23] and a new beam-angle (BA) method[33] for the respective measurements of a displacement vector and a displacement in an arbitrary direction (ie, an arbitrary directional displacement such as an axial, depth, lateral, or radial displacement).

Generally, BA data to be used with a conventional Doppler technique are used at values for performing analog or digital beamforming to generate the designed beams; that is, they are estimated by delays in the respective US elements. However, in real-world applications, the generated beam direction differs from the designed one because of the directivity of US transmission. Moreover, the beam direction changes in different positions because of the effects of scattering, reflection, and attenuation (ie, the beam direction also suffers from frequency modulations). Accurate BA data are obtained either through the evaluation of the position of the first moment of local spectra or from evaluation of instantaneous frequencies.[33] If a direction of the target motion can be determined, the BA method permits a highly accurate measurement of an arbitrary directional displacement. When performing ASTA, for instance, blood flow in vessels running parallel to the body surface (eg, in the carotid artery) can be measured with very high accuracy. Specifically, the most popular 1D AM[3] and the 1D AM and DM[13,19,22,31] or SFDM,[23,31] with multidimensional moving average methods, are similar to those used in MAM or MDM,[13,31] and can be used to yield a more accurate lateral displacement measurement with a simpler measurement technique than the lateral DM previously described[17,18,23]; that is, without a rotation of the coordinate system. However, the measurement accuracy obtained is lower than that obtained by the multidimensional methods with LM. Further, Sumi et al[33] show that the combination of the new BA method with 1D AM to create the so-called multiple crossed beams method with non-superimposed or separated beams[13,17,18,20,22] obtained from MTM[13,17,18,20,22,28,29] or MDSAM[13,17,18,20,22,30] is theoretically equivalent to MAM and LM; however, the combination requires more processing to yield the same displacement vector measurements. Thus, in terms of measurement accuracy, LM with MAM including the BA method is the most accurate or effective.

Alternatively, for single-beam scanning or plane-wave transmission (ie, simple beamforming methods),[18,23,31] when using SFDM, plural multidimensional (two- [2-] or three-dimensional [3D]) analytic signals (plural quasi-steered beams, or quasi-LM) can be generated by dividing a single quadrant or octant spectra in the corresponding frequency domain to enable the use of MAM or MDM. For instance, when using ASTA for beamforming, the number of methods available to obtain a displacement vector measurement other than from SFDM is limited (ie, limited to block-matching methods,[17,18] such as the multidimensional cross-spectrum phase gradient method, multidimensional CCM, the MAM, and the MDM using a block-matching method [referred to as MAMb[17,18] and MDMb,[17,18] respectively]). Moreover, the respective simulations described in Sumi[18] and Sumi et al[23] confirmed that SFDM yields a higher measurement accuracy than the block-matching methods, but it yields a lower measurement accuracy than the original LM method – that is, a tenfold larger standard deviation (SD). Basically, for SFDM with ASTA, the steered beams should be aimed in the direction of the target motion, which increases measurement accuracy in the displacement magnitude measurements, as does the use of 1D displacement measurement methods with ASTA, although, this decreases the accuracy of the displacement angle.[23] However, it was also confirmed that echo or coordinate rotation increases the measurement accuracy of the displacement vectors.[23] Originally, the combination of SFDM and a version of ASTA with non-steered, single-beam scanning (ie, conventional non-steered, single-beam scanning) was completely equivalent to the first version of MAM or MDM, with neither the original LM nor any physical beam steering,[11–13,23,31,33–35] and the use of laterally, symmetrically divided spectra (quasi-LM) permitted a more accurate axial displacement measurement than 1D AM or 1D DM, even with a multidimensional moving average.[13,19,22,31] However, the measurement accuracy obtained for a displacement vector measurement becomes lower than that obtained with the original LM method, because the generated lateral frequency is lower than that generated using the original LM method.[13,19,33–35]

Despite this, the use of single-beam scanning or a single plane-wave transmission should still be considered with simple beamforming methods. In this report, for example, with conventional non-steered, focused single-beam transmission/reception scanning, and with a high-speed non-steered single plane-wave transmission, as well as with non-steered, focused single-beam reception scanning

using a linear array-type transducer, several effective uses of the SFDM are demonstrated using agar phantom experiments.[34,35] For high-speed scanning of a target tissue with a rapid motion (eg, blood flow in a carotid artery) and the use of a 2D array-type transducer (for volumetric imaging/measurement and axial or depth compression/ stretching strain measurement/imaging, etc), plane-wave transmission[13,15,16] is effective. For a comparison, the original LM methods with respective transmissions of crossed, steered focused beams, and single non-steered or crossed, steered plane waves are also performed.

Initially, this study shows that the measurement accuracy of a displacement vector depends on the use of an apodization function – that is, a parabolic function used for the original LM versus a rectangular function (ie, with no apodization). Next, we show that for conventional non-steered beamforming, disregarding lateral low-frequency spectra generates an LM echo image, which, further, significantly increases the measurement accuracy of a displacement vector (quasi-LM).[18] Because the use of a rectangular apodization function (ie, no apodization) yields a larger bandwidth in a lateral direction than the use of a parabolic function, disregarding lateral low-frequency spectra is more effective for the use of a rectangular function than for the use of a parabolic function; thus, quasi-LM echo imaging with higher lateral frequency and measurement accuracy of a displacement vector are achieved. Also for the original LM, when using rectangular apodization (ie, no apodization), disregarding lateral low-frequency spectra is particularly effective. In addition, utilizing the interchangeability of cosine and sine modulations performed after completing beamforming is also used for single-beam scanning as well as with the original LM scanning method. Specifically, the cosine and sine modulations are respectively used for LM and quasi-LM imaging and displacement vector measurements.

This study concludes that it is possible, with the appropriate use of new SFDMs, for simple single-beam scanning or simple plural crossed-beam scanning with no apodization to achieve almost the same accuracy as the original LM scanning method with effective apodization.

Another new application of SFDM is also described in this study: it is shown that an incoherent superposition of the frequency-divided spectra reduces speckles.[35–37] As is well known, speckle reduction has been performed using the incoherent superposition of crossed, steered beams[38–43] or beams generated using different US frequencies.[44–46] The method's effectiveness is demonstrated through the use of agar phantom experiments.

New SFDMs
Disregarding lateral low-frequency spectra and applications for single-beam scanning

Figure 1 shows schematic drawings of 2D echo imaging and 2D displacement vector measurements with quasi-LM using a single focused beam, specifically, a non-steered, focused single beam. Figure 1A shows a schematic apodization function; that is, a 1D function with a symmetric peak in a lateral direction. Scanning using such a beamforming method is fundamental to medical US imaging and measurements (eg, Doppler measurements). When using this type of beamforming method, a new LM is obtained by filtering out lateral low-frequency spectra in a frequency domain,
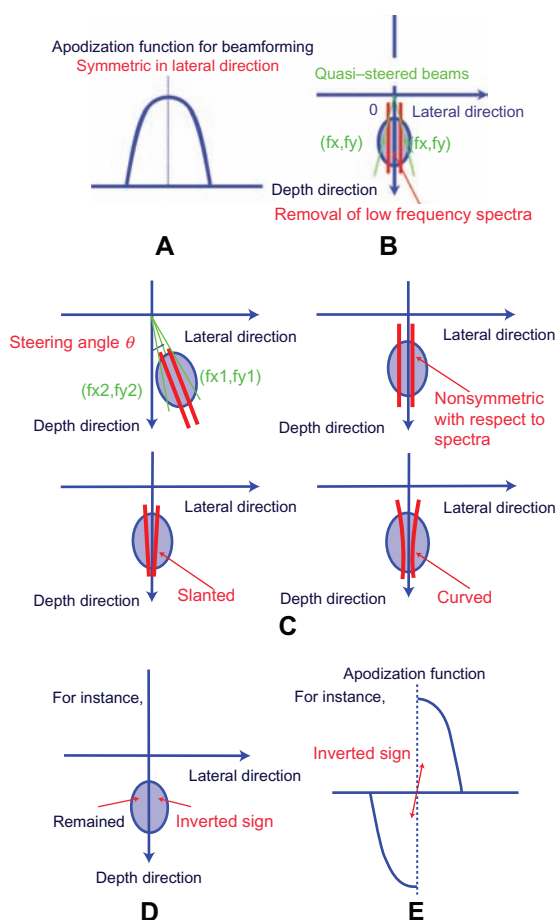

Figure 1 Schematics for two-dimensional imaging/measurement: (**A**) apodization function for non-steered single-beam scanning (ie, a one-dimensional function with a peak symmetric in a lateral direction); (**B**) lateral modulation (LM) achieved after performing such beamforming, ie, by filtering out lateral low-frequency spectra in a frequency domain; (**C**) examples of other methods for disregarding spectra for ASTA with a non-zero steering angle; use of a laterally non-symmetric boundary; use of slanted and curved boundaries etc; (**D**) interchangeability of cosine and sine LMs achievable, ie, by changing the sign of the spectra for either positive or negative lateral frequencies; (**E**) sine LM can also be achieved by using asymmetric apodization without lateral low-frequency filtering.
Note: The apodization function is not always symmetric with respect to the depth axis.

as shown in Figure 1B (the cutoff frequencies are ±f$_c$).[18,34,35] Strictly speaking, the new LM is achieved after completing the beamforming. For instance, when performing laterally symmetric filtering, as shown, the quasi-LM frequencies ±fy are obtained. That is, the inverse Fourier transforms of the two partial spectra yield two independent analytic signals expressing echo data with instantaneous frequencies (fx,fy) and (fx,-fy) generated by the synthesized, two symmetrically steered beams (ie, quasi-steered beams with quasi-steering angles ±θ).

In such a case, in a manner similar to that for the original LM method with physically steered beams with steering angles ±θ (see figure A1 in Sumi et al[23]), for the non-steered case (Figure 1B), the generated axial and lateral frequencies are expressed using the quasi-steering angles ±θ as follows:

$$fx = f_0 \cos \theta \quad \text{and} \quad fy = f_0 \sin \theta, \qquad (1)$$

where f$_0$ is a generated US frequency. If required, f$_0$ and θ can be estimated using the BA method.[33] The spectra distribution has properties such that when the axial frequency is high, the lateral frequency is low, and vice versa.

The new processing method then permits the use of the previously developed MAM[11–13] or MDM[11–13] for measurements of 2D displacement vectors as well as LM echo imaging. That is, after performing conventional non-LM beamforming, the quasi-LM echo data can be generated. Accordingly, a 2D displacement vector measurement (dx,dy) is also obtained at each point of interest by solving the following simultaneous equations:

$$f_x d_x + f_y d_y = c_1$$
$$f_x d_x - f_y d_y = c_2, \qquad (2)$$

where c$_1$ and c$_2$ are temporal instantaneous phase changes generated between the respective analytic signals obtained from subsequent scanning with the same non-LM beamforming method. Because in real-world applications, the generated beams are not laterally symmetric due to the actual directivity of US transmission, and to the inhomogeneities of the acoustical properties of a target tissue (eg, propagation speed, reflectivity, and attenuation), the absolute axial instantaneous frequencies and the absolute lateral instantaneous frequencies are different, respectively.[33] However, the MAM and MDM use the estimates of the axial and lateral frequencies (ie, generated quasi-steering angles ±θ).[11–13,33]

Note that when not disregarding any spectra, the original SFDM[18,23,33] can be used for a displacement vector measurement; that is, the first version of MAM or MDM

with neither LM nor any physical beam steering,[11–13,23,31,33–35] and the use of laterally, symmetrically divided spectra permits a more accurate measurement of an axial or depth displacement component than the 1D AM or 1D DM, even with a multidimensional moving average.[31] Strictly speaking, the laterally symmetrically divided spectra can be obtained by ignoring the lateral direct current (DC). Although the lateral DC has a high echo signal-to-noise ratio (SNR), ignoring it yields more accurate measurements. Although displacement measurements can also be performed using the SFDM without ignoring any spectra, ignoring the spectra around the boundary for the spectra division must be done, at least to obtain a quasi-LM image. In contrast, as the absolute cutoff frequency, f$_c$, increases from 0 Hz, the absolute quasi-steering angle θ and the lateral frequency f$_y$ increase simultaneously. As shown by simulations in Sumi,[13] high accuracy in axial and lateral displacement measurements is achieved by using a higher frequency US and/or a larger steering angle. There is also an increase in the independence of the simultaneous equations (Equation 2). Moreover, particularly when the spatial frequency of a target displacement distribution is low (ie, the distribution is continuous or smooth), the simultaneous decrease in the lateral bandwidths of the quasi-steered beams (ie, the broadening of the quasi-steered beam widths) is not sensitive to measurement accuracy.[13] However, an excessive disregard of the central spectra decreases the echo SNR significantly and, subsequently, the accuracy of a displacement vector measurement, as will be demonstrated later in this paper in an agar phantom experiment.

The new processing method can also be performed with ASTA[17,18] beamforming – that is, with a non-zero steering angle. This can be understood by recalling the application of the original SFDM to ASTA.[18,23,33] For instance, as shown in the top left panel of Figure 1C, by disregarding the central spectra existing in the direction of the steered beam, equation 1 in Sumi et al[23] will be more independent (the obtained frequencies are fx1, fy1, fx2, and fy2, as depicted). Further, in figure 1 in Sumi et al,[23] the schematics of ASTA and SFDM without ignoring spectra are shown. However, the decreases in an echo SNR and the bandwidth must also be considered. Measurements using ASTA will be reported elsewhere. In conjunction with several spectra division methods described in Sumi et al,[23] various methods for disregarding or ignoring spectra can be considered. For instance, as shown in Figure 1C (excluding the top left panel), the boundary for ignoring or disregarding spectra may be non-symmetric (top right panel), slanted (lower left panel), or curved (lower right panel). Such disregard can also be used for ASTA (top left panel).

Proper windows should also be used in the frequency domain. The effective evaluation of such methods will be reported in detail elsewhere.

In the agar phantom experiments shown following, for transmission and reception apodizations for a depth x, a parabolic function $A_p(y)$ was used (ie, parabolic apodization) as follows:

$$A_p(y) = \begin{cases} \dfrac{1}{2\lambda x}\left[-\dfrac{4\sigma_y^2\pi^2}{9}\left(\dfrac{y}{\lambda x}\right)^2 + 1\right] & \text{for} \quad -\dfrac{3\lambda x}{2\sigma_y\pi} \leq y \leq \dfrac{3\lambda x}{2\sigma_y\pi} \\ 0 & \text{for otherwise.} \end{cases}$$

$$(3)$$

For comparison, a non-parabolic apodization was also performed using a rectangular window $A_r(y)$; that is, a rectangular apodization or no apodization,

$$A_r(y) = \begin{cases} \dfrac{1}{2\lambda x} & \text{for} \quad -\dfrac{3\lambda x}{2\sigma_y\pi} \leq y \leq \dfrac{3\lambda x}{2\sigma_y\pi} \\ 0 & \text{for otherwise.} \end{cases} \quad (4)$$

For transmission and reception focusing, spherical focusing was performed. These apodization functions have the same effective aperture width in which the half width $[(3\lambda x)/(2\sigma_y\pi)]$ yields an SD three times as large as that of a Gaussian apodization function:

$$A_g(y) = \begin{cases} \dfrac{1}{2\lambda x}\exp\left[-\dfrac{(2\pi\sigma_y)^2}{2}\left(\dfrac{y}{\lambda x}\right)^2\right] & \text{for} \quad -\dfrac{3\lambda x}{2\sigma_y\pi} \leq y \leq \dfrac{3\lambda x}{2\sigma_y\pi} \\ 0 & \text{for otherwise,} \end{cases}$$

$$(5)$$

which is obtained as a Fraunhofer approximation of a Gaussian-type lateral point spread function (PSF) with an SD σy:

$$\exp\left[-\dfrac{y^2}{2\sigma_y^2}\right]. \quad (6)$$

As explained in Sumi et al,[15] a parabolic apodization yields a higher echo SNR than a Hanning apodization or a Gaussian apodization. This is confirmed by the fact that it has a larger full width at half maximum and shorter feet than other windows and functions when the transmitted US intensity is the same (see figure 1 in Sumi et al[15]). Accordingly, as will be confirmed, the rectangular apodization function, Equation 4, yields a larger transmission US intensity and a larger lateral bandwidth than the parabolic apodization function, Equation 3. As a rectangular apodization yields a larger lateral bandwidth than a parabolic apodization when using the same physical aperture or sub-aperture, the effectiveness of the new SFDM method is notable for its rectangular apodization, both for a high spatial resolution quasi-LM echo imaging and a simultaneous high accuracy in displacement vector measurements.

In Sumi et al,[23] for ASTA with a non-zero steering angle, the proper rotation of echo data or coordinate systems was effective in increasing displacement vector measurement accuracy, but the proper apodization function should be sought. Although apodization functions can also be designed simply by rotating Equations 2 to 4 with the steering angle, the most effective function must be determined by considering the actual directivity of US transmission from the transducer elements. For instance, as is well known, the rectangular apodization function is not appropriate with a large steering angle (also shown in the agar phantom experiments). Appropriate functions can be determined using previously described optimal methods.[47–49]

By comparison, in the agar phantom experiments, apodization and focusing were not used for transmission (ie, a non-apodized plane wave was used). The corresponding new 3D measurements/imaging using lateral and elevational modulations are described in the Appendix, and experimental data will be reported elsewhere.

Interchangeability of cosine and sine LMs and applications for single-beam scanning

In Figure 1D, interchangeability of cosine and sine LMs is shown; that is, that obtainable by changing the sign of the spectra of either the positive or negative lateral frequency. The relation can be simply confirmed from the fact that cosine LM can be achieved using laterally symmetric apodization (Figure 1A) and lateral low-frequency filtering (Figure 1B) and sine LM can be achieved using laterally asymmetric apodization (Figure 1E) and lateral low-frequency filtering (Figure 1B). For instance, by changing the sign of either partial spectra (ie, one of the divided spectra) after performing cosine LM beamforming (Figure 1A and B), the sine LM can be obtained (Figure 1E and B) with almost the same lateral frequencies. In contrast, after performing sine LM beamforming (Figure 1E and B), the corresponding cosine LM can also be obtained. Both LMs can be obtained after completing conventional non-LM beamforming.

Note that although the cosine LM requires absolute disregard of the lateral DC (Figure 1B), the sine LM does not always require such a disregard of spectra, even for quasi-LM imaging (Figure 1E), if a laterally asymmetric distribution

of spectra is obtained. As will be shown further on in the agar phantom experiments, as the sine LM yields a slightly higher LM frequency than the corresponding cosine LM, the sine LM is useful for displacement vector measurements, whereas the cosine LM is particularly useful for LM imaging because the target is presented in a spatial position in the obtained echo image. The detection methods are mentioned further on. The reason why the sine LM modulation yields a higher LM frequency than the corresponding cosine LM modulation is that the PSF has a zero crossing at a laterally central position. This is particularly effective when a lateral narrow beam is generated – that is, when a large lateral bandwidth with a lateral DC and very low lateral frequency spectra are generated (eg, when performing non-steering and, interestingly, the original LMs with rectangular apodization). This will be demonstrated in the agar phantom experiments. Together with the quasi-LM echo imaging and simultaneous displacement vector measurements, conventional non-LM imaging and measurements can also be performed. Corresponding new 3D measurement/imaging using lateral and elevational modulations is described in the Appendix (experimental data will be reported elsewhere).

Applications for the original LM using physically crossed plural beams

It should be noted that the two new processing steps (ie, disregarding lateral low-frequency spectra and interchanging cosine and sine LMs) can also be applied to the original methods for LM echo imaging and LM displacement vector measurements.[11–16] Figure 2A and B show the corresponding cosine and sine LMs; that is, with almost the same LM frequencies. As shown in Figure 2C, these are also similarly interchangeable in a frequency domain by changing the sign of either spectra with plus and minus lateral frequencies. In addition, as shown in Figure 2D, disregarding the lateral low-frequency spectra (cutoff frequencies, $\pm f_c$) increases the LM frequencies (ie, $\pm f_y$), although the lateral bandwidth decreases. Echo SNRs should also be considered. Increases in the independence of the simultaneous equations for MAM or MDM (equations 1 and 2 in Sumi[13]) are expected. However, as will be shown in the agar phantom experiments, when previously confirmed appropriate apodization functions using parabolic functions[15,16] were used, the effectiveness was not confirmed. An appropriate disregard should also be considered for the apodization function used.

In the agar phantom experiments shown following for cosine LM with a LM frequency f_y, for transmission and
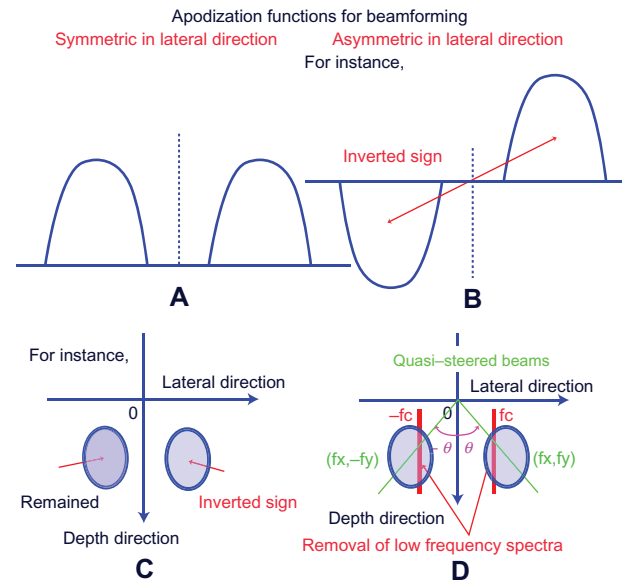

Figure 2 Schematics for a two-dimensional case: apodization functions (**A**) for the original cosine lateral modulation (LM) beamforming achieved by superposing crossed, steered beams (ie, a one-dimensional function with two peaks symmetric in a lateral direction) and (**B**) for the original sine LM beamforming (ie, a one-dimensional function with two peaks asymmetric in a lateral direction); (**C**) interchangeability of cosine and sine LMs achievable (ie, by changing the sign of the spectra of either the positive or negative lateral frequency); (**D**) increasing the lateral modulation frequency achieved after performing an original LM (ie, by filtering out lateral low-frequency spectra in a frequency domain).
Notes: Such an apodization symmetric with respect to the depth axis is not always performed (not shown). The direction of modulation may also be slanted (not shown).

reception apodizations for a depth x, parabolic functions $A_{pl}(y)$ (Sumi et al,[15] a parabolic apodization) and rectangular windows $A_{rl}(y)$ (a rectangular apodization) were used as follows:

$$
A_{pl}(y)
= \begin{cases}
\dfrac{1}{2\lambda x}\left[-\dfrac{4\sigma_y^2\pi^2}{9}\left(\dfrac{y}{\lambda x}+f_y\right)^2+1\right] & \text{for } -f_y\lambda x-\dfrac{3\lambda x}{2\sigma_y\pi} \le y \le -f_y\lambda x+\dfrac{3\lambda x}{2\sigma_y\pi} \\[2mm]
\dfrac{1}{2\lambda x}\left[-\dfrac{4\sigma_y^2\pi^2}{9}\left(\dfrac{y}{\lambda x}-f_y\right)^2+1\right] & \text{for } f_y\lambda x-\dfrac{3\lambda x}{2\sigma_y\pi} \le y \le f_y\lambda x+\dfrac{3\lambda x}{2\sigma_y\pi} \\[2mm]
0 & \text{for otherwise,}
\end{cases}
$$

$$(7)$$

$$
A_{rl}(y) = \begin{cases}
\dfrac{1}{2\lambda x} & \text{for } -f_y\lambda x-\dfrac{3\lambda x}{2\sigma_y\pi} \le y \le -f_y\lambda x \dfrac{3\lambda x}{2\sigma_y\pi} \\[2mm]
\dfrac{1}{2\lambda x} & \text{for } f_y\lambda x-\dfrac{3\lambda x}{2\sigma_y\pi} \le y \le f_y\lambda x \dfrac{3\lambda x}{2\sigma_y\pi} \\[2mm]
0 & \text{for otherwise.}
\end{cases} \qquad (8)
$$

These apodization functions have two symmetric parabolic and rectangular peaks for which the half widths (ie, the

half-effective aperture widths) are the same $[(3\lambda x)/(2\sigma_y\pi)]$ and which yield an SD three times as a large as the Gaussian apodization function:[15]

$$A_{gl}(y)$$

$$= \begin{cases} \frac{1}{2\lambda x}\exp\left[-\frac{(2\pi\sigma_y)^2}{2}\left(\frac{y}{\lambda x}+f_y\right)^2\right] \\ \qquad \text{for} -f_y\lambda x-\frac{3\lambda x}{2\sigma_y\pi}\le y\le -f_y\lambda x+\frac{3\lambda x}{2\sigma_y\pi} \\ \frac{1}{2\lambda x}\exp\left[-\frac{(2\pi\sigma_y)^2}{2}\left(\frac{y}{\lambda x}-f_y\right)^2\right] \\ \qquad \text{for} \ f_y\lambda x-\frac{3\lambda x}{2\sigma_y\pi}\le y\le f_y\lambda x+\frac{3\lambda x}{2\sigma_y\pi} \\ 0 \qquad\qquad \text{for otherwise} \end{cases}$$

(9)

which is obtained as a Fraunhofer approximation[13] of a Gaussian-type lateral PSF with an SD σ_y; that is,

$$\exp\left[-\frac{y^2}{2\sigma_y^2}\right]\cos(2\pi f_y y).$$ (10)

For transmission and reception focusing, spherical focusing was performed. To generate a LM frequency with a frequency of half of the US frequency (7.5 MHz), steering angles were set at ±14.0 degrees. To compensate for the LM frequency and lateral bandwidth that would be smaller than designed values (the generated steering angles were ±11.8 degrees for parabolic apodization), compensation parameters were introduced in Sumi,[13] Sumi et al,[15] and Sumi and Tanuma,[16] but these uses are beyond the scope of this report. Note also that all the apodization functions Equations 6 to 8 use the corresponding functions Equations 2 to 4 with the same effective aperture symmetrically, that is, for the respective steered beams. Thus, the effective aperture sizes for original LM with crossed beams are more than twice the size present in the corresponding non-steered beamforming.

In the agar phantom experiments for the original LMs (shown following), as for the non-steered cases, rectangular apodization (Equation 8) yielded a larger lateral bandwidth than parabolic apodization (Equation 7), and, however, smaller steering angles were obtained. Accordingly, accuracy in the displacement vector measurements decreased. When obstacles such as bones exist, the crossed beams may also be generated non-symmetrically with respect to the depth axis (not shown in Figure 2).[17,18,23] Similarly, in the ASTA case with a non-zero steering angle (as already mentioned), the proper apodization function should be determined using an optimization method previously developed,[47–49] although apodization functions can also be designed by simply using

a coordinate rotation of Equations 6 to 8. Alternatively, the echo data or coordinate system may be rotated properly.[23] Laterally internal spectra should also be disregarded.

In the agar phantom experiments (shown following), for comparison, no apodization was used with plane-wave transmissions with non-steering and steering (ie, non-apodized plane waves were used with non-steering and steering). Although when such non-apodized plane waves are transmitted instead of the spherical-focused beams, the apodization for the reception of spherical-focused beams should be performed with Gaussian functions with long feet rather than with parabolic functions with short feet (see Sumi et al[15] and Sumi and Tanuma[16]), and the appropriate apodization was not performed in this report. The corresponding new 3D measurements/imaging using lateral and elevational modulation are described in the Appendix (experimental data will be reported elsewhere).

Applications for LM echo imaging and speckle reduction

In conjunction with the new SFDMs, LM (or quasi-LM) echo imaging and echo speckle reduction can be achieved by performing coherent and incoherent superposition of divided (ie, divisions) or original spectra.[35–37,50–52] For instance, with the original LM with physically crossed beams (Figure 2), B-mode LM echo imaging has been reported.[15,16] Moreover, speckle reduction has been achieved using incoherent superposition of physically steered beams[38–43] and beams generated using different US frequencies.[44–46]

This group's coherent and incoherent superposition for such imaging is performed using multidimensional signals.[35–37,50–52] To obtain plural quasi-steered beams from a steered or non-steered single beam, spectra frequency division can be performed as shown in Figure 1. Further, with the original LM using physically crossed beams, if required, the spectra frequency division can be similarly performed on a single quadrant or octant spectra to increase the number of beams. For generating an incoherent signal, envelope and square detection are useful.

For a physically transmitted/received beam, with a synthesized aperture beam and a synthesized beam using SFDM or coherent superposition,[50–52] one raw rf-echo signal or one analytic signal can be obtained. For an analytic signal R + jI (R, real part; I, imaginary part; j, imaginary unit), envelope detection[37] can be simply accomplished (i) by performing quadrate detection or (ii), calculating $\sqrt{R^2+I^2}$ or R^2+I^2. Although the quadrate detection (i) can also be performed on digitized multidimensional (3D or 2D) and 1D signals using appropriate cosine and sine functions

with a plus or minus carrier frequency (ie, the first moment or instantaneous frequency in one of the directions of the coordinate axes), (ii) is more effective than (i), particularly when the digitized signal is Fourier transformed (the analytic signal can be obtained by performing the inverse Fourier transform of the divided, superposed, or physically generated single quadrant or octant spectra). Otherwise, for instance, (iii) the corresponding spectra can be shifted in a frequency domain using the estimated first moments or instantaneous frequencies, after which a base-band signal A + jB (A, real part; B, imaginary part; j, imaginary unit) is obtained by performing an inverse Fourier transform and calculating $\sqrt{A^2 + B^2}$ or $A^2 + B^2$, or (iv) multiplication is performed with respect to the analytic signals obtained through the inverse Fourier transform of the divided, superposed, or physically generated single quadrant or octant spectra that are symmetric with respect to the origin and have the inverse signs of the same absolute instantaneous phase. However, when the spectra are estimated not from local raw echo data but from global raw echo data, (iii) yields inaccurate results, and both (iii) and (iv) require more processing than (ii). Thus, (ii) is the best envelope-detection method.

In contrast, square detection requires simpler calculations than envelope detection. For the digitized raw rf-echo signal or the real or imaginary part of the analytic signal (when expressed by S), the detected signal is obtained as $\sqrt{S^2}$ or S^2.

Then, for respective detection (ie, envelope and square detection), the superposition of incoherent signals (the number of beams or signals, N) is obtained as:[35–37,50–52]

$$\sum_{i=1}^{N} \sqrt{(R_i^2 + I_i^2)} \quad \text{or} \quad \sum_{i=1}^{N} (R_i^2 + I_i^2) \qquad (11)$$

$$\text{and} \quad \sum_{i=1}^{N} \sqrt{S_i^2} \quad \text{or} \quad \sum_{i=1}^{N} S_i^2. \qquad (11')$$

For LM echo imaging, the detection of superposed N coherent signals (or N beams) is used:[35–37,50–52] for the respective detection,

$$\sqrt{\left(\sum_{i=1}^{N} R_i\right)^2 + \left(\sum_{i=1}^{N} I_i\right)^2} \quad \text{or} \quad \left(\sum_{i=1}^{N} R_i\right)^2 + \left(\sum_{i=1}^{N} I_i\right)^2 \qquad (12)$$

$$\text{and} \quad \sqrt{\left(\sum_{i=1}^{N} S_i\right)^2} \quad \text{or} \quad \left(\sum_{i=1}^{N} S_i\right)^2. \qquad (12')$$

However, when a small number N is obtained, such as when performing LM (ie, for a 2D imaging/measurement

case, N = 2; for a 3D case, N = 3 or 4), the imaging results obtained using the incoherent and coherent superposition are almost same; that is, Equations 11 and 12 (envelope detection), and Equations 11′ and 12′ (square detection), respectively, are used. In such a case, the effect of speckle reduction using incoherent superposition (Equations 11 and 11′) is not intense, particularly when using square detection (Equation 11′). On the contrary, for LM echo imaging, the superposition of incoherent signals obtained by the square detection (Equation 11′) may be more useful than the square detection of coherent superposition (Equation 12′). This is because US oscillations cannot be found in the echo images obtained through envelope detection (Equations 11 and 12) and when using the incoherent superposition (Equations 11 and 11′), the specular echo signals generated by phenomena such as strong scattering and reflection are amplified and can be more clearly visualized than when using the coherent superposition (Equation 12 or 12′). Actually, the B-mode images shown previously for LM echo imaging using physically crossed beams include such obtained images (eg, Sumi et al[15] and Sumi and Tanuma[16]). For coherent and incoherent superposition, original raw echo data can also be used.

For imaging with incoherent superposition for a deep region, the summation processing in Equations 11 and 11′ should be performed on the amplitude signals rather than on the power signals. Incoherent superposition may also be performed on the higher order power signals instead with Equation 11′ (ie, greater than second order), but images obtained this way will not be useful for a deep region in such a case. This is also true when performing incoherent superposition for speckle reduction.

In contrast, for speckle reduction, a large number of beams or quasi-beams with different steering angles are used. As mentioned, speckle reduction can be performed for an arbitrary beamforming. When using SFDM for speckle reduction, division can also be performed using the horizontal lines as shown in Figure 3A (ie, a horizontal division) in addition to the vertical lines (ie, a vertical division) as shown in Figure 3B, as for SFDM as shown in Figure 1. This can be done either independently (as shown in Figure 3A and B) or simultaneously (not shown). That is, such obtained partial spectra (divisions) are detected and superposed on divisions obtained using either only the horizontal division, only the vertical division, or both the horizontal division and vertical division, and performed independently or simultaneously. Further, horizontal or vertical planes can be used for 3D imaging (see Appendix)
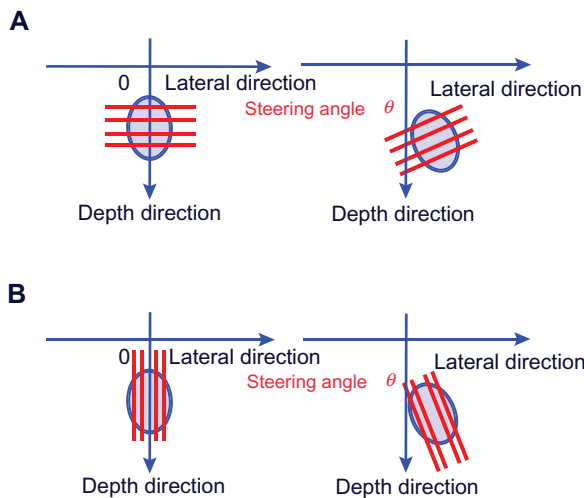
Figure 3 Schematics of (**A**) horizontal and (**B**) vertical divisions for a non-steered beam, ASTA, or lateral modulation for a two-dimensional case; for instance, when five partial divided spectra are obtained by four divisions.

and a number of vertical or horizontal lines or planes can be used. The lines and planes can be slanted or curved. As shown in the agar phantom experiments, detailed following, the simultaneous plural vertical and horizontal divisions are effective, although the spatial resolution decreases due to the decrease in bandwidth.

In this report, the focus is on the use of square detection rather than envelope detection with the original LM and quasi-LM imaging and speckle reduction. Speckle reduction

using SFDM is shown only for single-beam scanning. The use of envelope detection will be reported in detail elsewhere together with speckle reduction using the original LM method with plural physically generated beams. The original LM and quasi-LM imaging methods and speckle reduction for 3D imaging (see Appendix) will be reported elsewhere.

Agar phantom experiments

For 2D imaging/measurements, the same agar phantom was used as previously.[15,16,19,23,33] The rectangular region of interest (ROI), with dimensions of 13.7 (depth) × 13.2 (lateral) mm, was set at a depth of 12.2 mm using a linear array-type transducer. A central circular region (a cylindrical inclusion with a diameter of 10 mm and a depth of 19 mm) had a larger shear modulus than the surrounding region – that is, a relative value of 3.29 (2.63 vs 0.80×10^6 N/m^2). The agar phantom was compressed in the lateral direction. Synthetic aperture data were acquired using a nominal US frequency of 7.5 MHz.

Ten different beamforming methods were defined using different focusing methods and different apodization methods as summarized in Table 1, and are referred to as Methods A to J.

The focusing methods used were described as F(tr,re), where "tr" and "re" are abbreviations for transmission and reception, respectively, of US. For US transmission (tr),

Table 1 Beamforming methods A to J

Method	Focusing F(tr,re)	Parabolic apod A(tr,re)	Explanation of beamforming
A	F(spx2,spx2)	A(tr,re)	Parabolic LM using two crossed, steered spherical-focused beam transmissions and receptions
B	F(plx2,spx2)	A(re)	Parabolic LM using two crossed, steered plane-wave transmissions and two crossed, steered spherical-focused beam receptions
C	F(plx1,spx2)	A(re)	Parabolic LM using single non-steered plane-wave transmission and two crossed, steered spherical-focused beam receptions
D	F(spx2,spx2)	A(–)	Rectangular LM using two crossed, steered spherical beam transmissions and receptions
E	F(plx2,spx2)	A(–)	Rectangular LM using two crossed, steered plane-wave transmissions and two crossed, steered spherical-focused beam receptions
F	F(plx1,spx2)	A(–)	Rectangular LM using single non-steered plane-wave transmission and two crossed, steered spherical-focused beam receptions
G	F(spx1,spx1)	A(tr,re)	Parabolic quasi-LM using single non-steered, spherical-focused beam transmission and reception
H	F(plx1,spx1)	A(re)	Parabolic quasi-LM using single non-steered plane-wave transmission and single non-steered, spherical-focused beam reception
I	F(spx1,spx1)	A(–)	Rectangular quasi-LM using single non-steered, spherical-focused beam transmission and reception
J	F(plx1,spx1)	A(–)	Rectangular quasi-LM using single non-steered plane-wave transmission and single non-steered, spherical-focused beam reception

Abbreviations: LM, lateral modulation; apod, apodization; tr, transmission; re, reception; sp, spherical focusing using spherical waves; pl, non-focusing using plane waves; x1 and x2, non-crossed single and two crossed waves, respectively; F(tr,re), focusing using sp or non-focusing using pl for tr and re; A(tr and/or re), parabolic apodization for tr and/or re; A(non-described tr or re, or described as –): non-parabolic apodization using a rectangular window for tr or re, or both tr and re, ie, rectangular apodization or no apodization.

either a non-focused plane wave, described as "pl," or a spherical-focused beam, described as "sp," was used. For US reception (re), only a spherical-focused beam was used (ie, dynamic focusing was performed). Specifically, using such a plane wave and/or a spherical-focused beam, non-steered single-beam scanning and the original LM scanning using two crossed, steered beams were used, and these were denoted by "x1" and "x2," respectively. Summarizing, respective tr and re are "spx1," "spx2," "plx1 (only for tr)" or "plx2 (only for tr)." Thus, for tr and re, four kinds of scanning were performed using a non-steered, single spherical-focused beam (spx1), two crossed, steered spherical-focused beams (spx2), a non-steered, single plane wave (plx1 only for tr), or two crossed, steered plane waves (plx2 only for tr).

For apodization, parabolic and rectangular apodizations were performed, both for non-steered single-beam scanning (Equations 3 and 4) and for the original LM method scanning (Equations 7 and 8). When using pl for tr (ie, plx1 or plx2), no apodization was performed. For a spherical-focused beam, either of two apodizations was performed. As mentioned, because the rectangular apodization is equivalent to no apodization, hereafter, parabolic apodization used for tr and re is denoted by "A(tr,re)" and rectangular apodization for tr or re is denoted by "–" for tr or re in A(tr,re) (see Table 1). In Equations 3, 4, 7, and 8, σ_y was set at 0.4 mm. When using the Fraunhofer approximation, this corresponds to a case when the beam width was designed so that 99.7% of the US energy exits within a 2.4 mm (=$\sigma_y \times 6$ mm) width. The LM frequency was designed to be 3.75 MHz (half the US frequency).

Evaluation of raw spectra

To confirm the generated beam widths and LM frequencies (Methods A to J), the obtained 2D spectra (shown in Figure 4) were analyzed. At first, the resulting raw spectra were examined. For Methods A to C, the original LM method was used with parabolic apodization: specifically, A(tr,re), A(re), and A(re), respectively.[15] That is, for all of the methods, parabolic apodization was performed at least for re. Because Methods A to C were used with spx2, plx2, and plx1 for tr, respectively, with spx2 for re, the order of the size of the lateral bandwidth became A (maximum frequency, 5.7; minimum frequency, 0.3 = 5.4 MHz) > B (5.4 – 0.9 = 4.5 MHz) > C (3.3 MHz). Interestingly, the order of the lateral frequency was different from that of the lateral bandwidth: B (3.12 MHz) > A (2.92 MHz) > C (1.55 MHz). The use of plx2 (Method B) yielded a higher lateral frequency than spx2 (Method A), although a smaller lateral bandwidth was obtained.

As clarified from the simulations in Sumi,[13] higher axial and lateral frequencies yielded higher accuracies for the axial and lateral displacement measurements. In addition, the axial and lateral bandwidths are not sensitive to measurement accuracy (specifically, because the accuracy of a lateral displacement measurement is significantly lower than that of an axial displacement measurement, an increase in the accuracy of the lateral displacement measurement is required in general).[13] However, as shown in Sumi,[13] Sumi et al,[15] and in this report, the use of the focusing method F(plx2,spx2) (ie, Method B) yielded a lower measurement accuracy than that of F(spx2,spx2) (ie, Method A). This is due to a lower echo SNR obtained using Method B [A(re) and F(plx2,spx2)] than was obtained when using Method A [A(tr,re) and F(spx2,spx2)]. Method C yielded the lowest measurement accuracy due to the lowest lateral frequency generated, the smallest lateral bandwidth and a low-echo SNR obtained with the use of plx1 for tr and A(re). Being different from Methods A and B, Method C yielded a lateral DC and very low lateral frequency spectra.

For the Methods D to F, the original LMs were performed using rectangular apodization [ie, no apodization, A(-)]. Corresponding to Methods A to C used with parabolic apodization, Methods D to F were used with spx2, plx2, and plx1 for tr, respectively, with spx2 for re and the order of the size of the lateral bandwidths was A (6.6 MHz) > B (5.7 MHz) > C (3.6 MHz); that of the lateral frequency became B (2.89 MHz) > A (2.16 MHz) > C (1.45 MHz). The orders of the size of the lateral bandwidth and the lateral frequency were the same as those for parabolic apodization (Methods A to C). This is due to the scheme used for beamforming (ie, the focusing methods). However, rectangular apodization yielded larger lateral bandwidths than parabolic apodization with the same focusing methods [eg, for the focusing method F(spx2,spx2), Method D's was 6.6 MHz vs Method A with 5.7 MHz]. Interestingly, the axial bandwidths were also larger than those obtained using parabolic apodization [eg, Method D with 7.7 (=11.1 – 3.4) MHz vs Method A with 7.4 (=10.5 – 3.1) MHz]. Although the larger lateral bandwidths were obtained due to rectangular apodization, the lateral frequencies were lower than with the corresponding Methods A to C (ie, Method D with 2.16 MHz vs Method A with 2.92 MHz; Method E with 2.89 MHz vs Method B with 3.12 MHz; Method F with 1.45 MHz vs Method C with 1.55 MHz). In contrast, the axial frequencies were higher (7.10 vs 6.96 MHz; 7.01 vs 6.97 MHz; 7.16 vs 7.16 MHz, respectively), because steering angles larger than those obtained using parabolic apodization
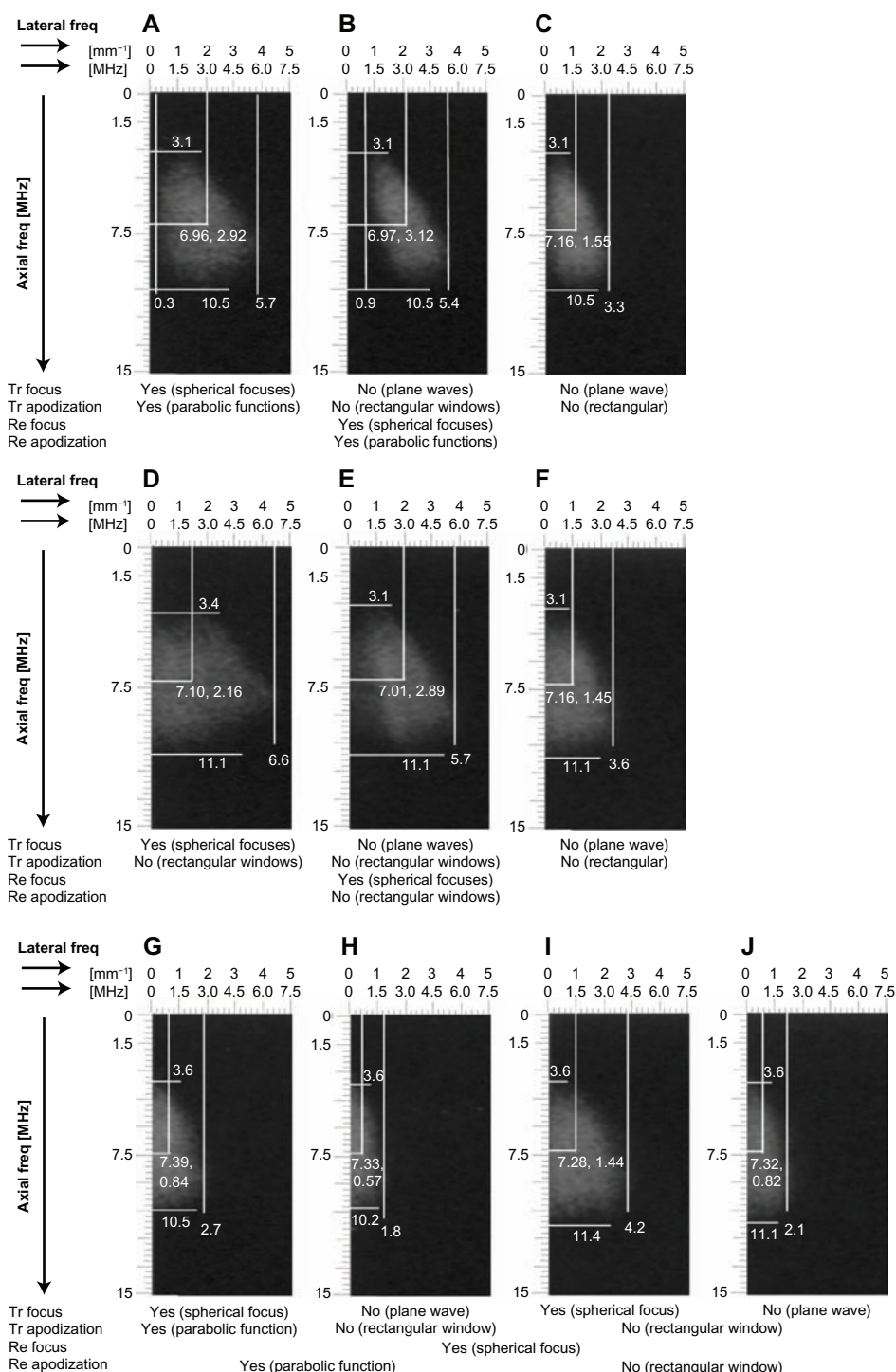
Lateral freq

A

[mm⁻¹] 0 1 2 3 4 5
[MHz] 0 1.5 3.0 4.5 6.0 7.5

Axial freq [MHz]

3.1
6.96, 2.92
0.3   10.5   5.7

Tr focus — Yes (spherical focuses)
Tr apodization — Yes (parabolic functions)
Re focus
Re apodization

B

[mm⁻¹] 0 1 2 3 4 5
[MHz] 0 1.5 3.0 4.5 6.0 7.5

3.1
6.97, 3.12
0.9   10.5   5.4

No (plane waves)
No (rectangular windows)
Yes (spherical focuses)
Yes (parabolic functions)

C

[mm⁻¹] 0 1 2 3 4 5
[MHz] 0 1.5 3.0 4.5 6.0 7.5

3.1
7.16, 1.55
10.5   3.3

No (plane wave)
No (rectangular)

Lateral freq

D

[mm⁻¹] 0 1 2 3 4 5
[MHz] 0 1.5 3.0 4.5 6.0 7.5

Axial freq [MHz]

3.4
7.10, 2.16
11.1   6.6

Tr focus — Yes (spherical focuses)
Tr apodization — No (rectangular windows)
Re focus
Re apodization

E

[mm⁻¹] 0 1 2 3 4 5
[MHz] 0 1.5 3.0 4.5 6.0 7.5

3.1
7.01, 2.89
11.1   5.7

No (plane waves)
No (rectangular windows)
Yes (spherical focuses)
No (rectangular windows)

F

[mm⁻¹] 0 1 2 3 4 5
[MHz] 0 1.5 3.0 4.5 6.0 7.5

3.1
7.16, 1.45
11.1   3.6

No (plane wave)
No (rectangular)

Lateral freq

G

[mm⁻¹] 0 1 2 3 4 5
[MHz] 0 1.5 3.0 4.5 6.0 7.5

Axial freq [MHz]

3.6
7.39, 0.84
10.5   2.7

Tr focus — Yes (spherical focus)
Tr apodization — Yes (parabolic function)
Re focus
Re apodization — Yes (parabolic function)

H

[mm⁻¹] 0 1 2 3 4 5
[MHz] 0 1.5 3.0 4.5 6.0 7.5

3.6
7.33, 0.57
10.2   1.8

No (plane wave)
No (rectangular window)
Yes (spherical focus)

I

[mm⁻¹] 0 1 2 3 4 5
[MHz] 0 1.5 3.0 4.5 6.0 7.5

3.6
7.28, 1.44
11.4   4.2

Yes (spherical focus)
No (rectangular window)

J

[mm⁻¹] 0 1 2 3 4 5
[MHz] 0 1.5 3.0 4.5 6.0 7.5

3.6
7.32, 0.82
11.1   2.1

No (plane wave)
No (rectangular window)

Figure 4 Spectra obtained for beamforming with Methods (**A–J**) using transmission (tr) and reception (re) focusing and apodization, as summarized in Table 1.
Note: No apodization is equivalent to rectangular apodization.

cannot be obtained. As shown, a lateral DC and very low lateral frequency spectra were generated. Correspondingly, the echo images have no lateral oscillations, as will be shown later. Thus, rectangular apodization is not suitable for steered beamforming. This can also be confirmed through displacement vector measurements. The measurement accuracies obtained using Methods D to F were lower than those obtained using the corresponding Methods A to C (shown later). In Methods D to F, similarly to the use of parabolic apodization, the use of F(spx2,spx2) (ie, Method D) yielded a higher measurement accuracy than that of F(plx2,spx2) (ie, Method E), and Method F yielded the

lowest measurement accuracy. For Method D, disregarding the lateral low-frequency spectra achieved almost the same accuracy in measurements as those obtained using parabolic apodization (Method A), as will be shown later. For raw echo data, the existence of a lateral DC and very low lateral frequency spectra decreased the lateral frequencies, although the raw spectra also had high-frequency spectra. Because the effectiveness of disregarding spectra also depends on the distribution of spectra (SNRs of spectra, etc), this will be investigated in detail following.

When performing plane-wave transmissions (plx2 or plx1), the propagation direction of US waves can be controlled with a higher accuracy than in spherical-wave transmissions (spx2). That is, both for parabolic and rectangular apodizations, steered plane-wave transmissions (plx2) yielded larger steering angles than steered spherical-wave transmissions (spx2). The non-steered single plane-wave transmission (plx1) yielded the smallest steering angles. An increase in accuracy is a notable feature of the use of rectangular apodization: for parabolic apodization, Method A with 2.92 MHz [F(spx2,spx2)] vs Method B with 3.12 MHz [F(plx2,spx2)] vs Method C with 1.55 MHz [F(plx1,spx2)]; and for rectangular apodization, Method D with 2.16 MHz [F(spx2,spx2)] vs Method E with 2.89 MHz [F(plx2,spx2)] vs Method F with 1.45 MHz [F(plx1,spx2)]. Although the crossed plane-wave transmissions yielded higher lateral frequencies than the crossed spherical-wave transmissions, a lower measurement accuracy was obtained, as mentioned, and this will be shown in the phantom experiments. This was particularly notable for rectangular apodization (Method E); that is, very low measurement accuracy was obtained, although the differences in the lateral frequencies were larger than for parabolic apodization (for rectangular apodization, $2.89 - 2.16 = 0.73$ MHz; for parabolic apodization, $3.12 - 2.92 = 0.20$ MHz). This was due to a low-echo SNR. The non-steered single plane-wave transmissions yielded the lowest measurement accuracy of all, specifically, with rectangular apodization. Thus, inherently, the combined use of rectangular apodization with plane-wave transmissions is not useful.

Ideally, disregarding low-frequency spectra is effective for a large bandwidth with a high first moment or a high instantaneous frequency. Disregarding low-frequency spectra is particularly effective when they have low SNRs. For both the axial and lateral directions, the spectra distribution will be investigated later in this paper. However, as will be shown in the phantom experiments, although with the original LMs with a rectangular apodization (ie, with a lateral DC and very low lateral frequency spectra), lateral low-frequency spectra

had high SNRs, disregarding low lateral frequency spectra was effective – that is, Method D with F(spx2,spx2).

For non-steered cases, Method G uses spherical-wave transmission/reception [ie, F(spx1,spx1)] with parabolic apodization A(tr,re). Method H uses a plane-wave transmission and a spherical-wave reception F(plx1,spx1) with parabolic apodization A(re). When not using parabolic apodization [ie, rectangular apodization, the A(–)], Method I uses F(spx1,spx1), and Method J uses F(plx1,spx1). As shown, in a manner similar to that with the original LM cases, the use of a rectangular apodization [ie, A(–)] yielded larger lateral bandwidths (Methods I with 4.2 MHz and J with 2.1 MHz) than using parabolic apodization (Methods G with 2.7 MHz and H with 1.8 MHz). For the respective apodizations, the use of a plane wave [ie, F(plx1,spx1)] yielded narrower lateral bandwidths (Methods H and J) than using no plane wave (Methods G and I). Being dependent on the size of the lateral bandwidth, the lateral frequencies obtained using no plane wave (Methods G with 0.84 MHz and I with 1.44 MHz) were larger than those obtained using a plane wave (Methods H with 0.57 MHz and J with 0.82 MHz). As will be seen, the order of measurement accuracy was the same as that of the lateral frequency obtained: Method I > Method G > Method J > Method H. In the non-steering case, not using a plane wave (Methods I and G) yielded more accurate measurements than using a plane wave. However, as predicted, the measurement accuracy achieved was lower than when using the original LMs. All of the spectra have a lateral DC and very low lateral frequency spectra. As with the original LMs with rectangular apodization, disregarding lateral low-frequency spectra was effective, particularly for Methods I and G with F(spx1,spx1). Method I, with the new SFDM, achieved almost the same accuracy of measurement as was obtained with the original LM with parabolic apodization (Method A), although the lateral frequency was lower. This was due to the fact that with non-steered beamforming, high echo SNRs were obtained in a low-frequency range and were disregarded, but high echo SNRs were also obtained over a high-frequency range.

Figure 5 shows spectra moments, maxima minus moments, and moments minus minima of axial (Figure 5A) and lateral (Figure 5B) directions obtained with beamforming Methods A to J, which are summarized in Table 1 and shown in Figure 4. With the axial direction, when using parabolic apodization for both the original LM with F(spx2,spx2) (ie, Method A) and non-steering with F(spx1,spx1) (ie, Method G), maxima minus moments are smaller than moments minus minima. Thus, spectra are larger (the signal energies are more dense) for the high axial frequency range (>axial moments) than for
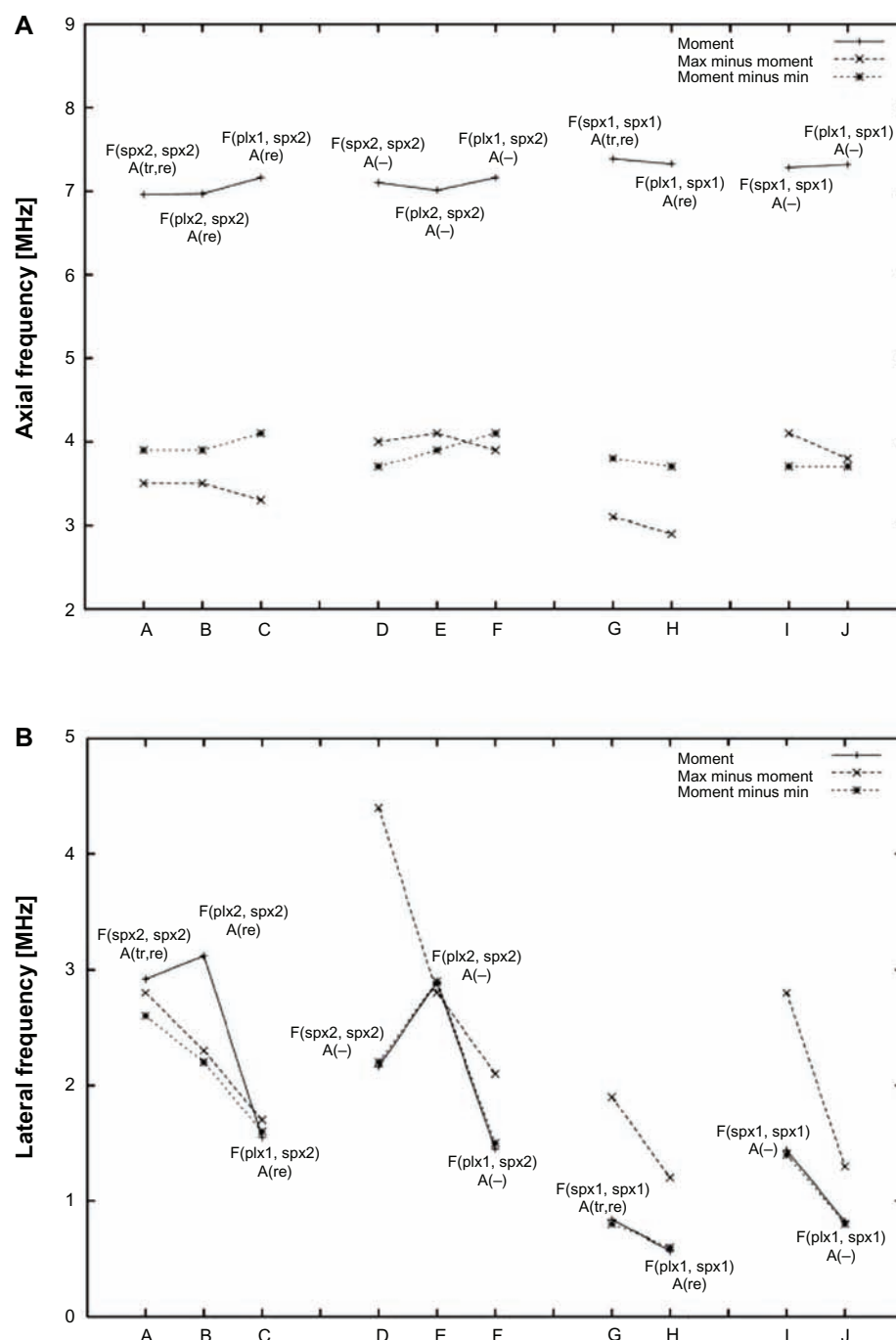
Figure 5 Spectra moments (center frequencies), maxima minus moments, and minima minus moments of (**A**) depth and (**B**) lateral directions obtained with beamforming Methods A to J as summarized in Table 1 and shown in Figure 4.

Abbreviations: tr, transmission; re, reception; sp, spherical focusing using spherical waves; pl, non-focusing using plane waves; x1 and x2, non-crossed single and two crossed waves, respectively; F(tr,re), focusing using sp or non-focusing using pl for tr and re; A(tr and/or re), parabolic apodization for tr and/or re; A(non-described tr or re, or described as –): non-parabolic apodization using a rectangular window for tr or re, or both tr and re (ie, rectangular apodization or no apodization).

the low axial frequency range (<axial moments). That is, the SNRs of the spectra are higher for the high axial frequency range than for the low axial frequency range. Thus, when using parabolic apodization, disregarding low axial frequency spectra is effective, although the results of this are not shown in this report. In contrast, when using rectangular apodization

for both the original LM with F(spx2,spx2) (ie, Method D) and non-steering with F(spx1,spx1) (ie, Method I), maxima minus moments are larger than moments minus minima. Thus, the SNRs of spectra are higher for the low axial frequency range than for the high axial frequency range. For the original LMs, the axial frequencies (axial first moments or

axial instantaneous frequencies) obtained using rectangular apodization are higher than those obtained using parabolic apodization; for the non-steering cases, the results are vice versa. The axial frequencies are larger for the non-steered cases than for the original LMs. For both the original LM and non-steered cases, the axial bandwidths are larger for rectangular apodization than for parabolic apodization.

Alternatively, regarding the lateral direction, when using parabolic or rectangular apodization for both, the original LM with F(spx2,spx2) (ie, Methods A and D), and with non-steering with F(spx1,spx1) (ie, Methods G and I), except that for the original LM with parabolic apodization (Method A) that yielded almost the same width for the high and low lateral frequency ranges, moments minus minima are smaller than maxima minus moments. Thus, spectra are larger (the signal energies are more dense) for the low lateral frequency range (less than lateral moments) than for the high lateral frequency range (greater than lateral moments). That is, the SNRs of the spectra are higher for the low lateral frequency range than for the high lateral frequency range. Thus, when using parabolic or rectangular apodization, disregarding the low lateral frequency spectra was an experiment, and measurement accuracy increased, as will be shown later. As confirmed earlier, for the original LM and non-steered cases, the lateral bandwidths as well as the axial bandwidths are also larger for rectangular apodization than for parabolic apodization (although, for the original LMs, the lateral frequency became smaller with rectangular apodization than with parabolic apodization, for the non-steered cases, and vice versa). Thus, disregarding low lateral frequency spectra was more effective for rectangular apodization than for parabolic apodization.

When using non-steered single plane waves for transmission for the respective original LM and non-steered cases (eg, Methods C, F, and J with plx1 for tr), the axial frequencies became larger than when using spherical-wave transmissions (eg, Methods A and D with spx2 for tr and Method I with spx1 for tr). In addition, the high and low axial frequency ranges became small and large, respectively (eg, Methods C, F, and H). The order of spectra SNRs became high > low axial frequency ranges. Thus, when performing non-steered single plane-wave transmission with parabolic or rectangular apodization for the original LM or non-steered cases, disregarding axial low-frequency spectra is also effective (the results are not shown in this report). Alternatively, the lateral frequencies (eg, Methods C, F, H, and J with plx1) became smaller than when using spherical waves for transmission (eg, Methods A and D with spx2 and Methods G and I with spx1). In addition, both the high and low lateral frequency ranges became small

(Methods C, F, H, and J). The order of spectra SNRs of high and low lateral frequency ranges did not change. That is, the low lateral frequency range also has a high SNR when using non-steered single plane-wave transmission. However (see the "LM and quasi-LM imaging" subsection and the "Measurements using LM and quasi-LM" subsection), disregarding lateral low-frequency spectra was also effective for the original LM and non-steered cases, particularly when using rectangular apodization (Method F vs C; Method J vs H).

When using crossed plane waves for the original LMs [ie, F(plx2,spx2)], the axial frequencies became smaller than when using crossed spherical waves [ie, F(spx2,spx2)], particularly when using rectangular apodization [ie, Method E using F(plx2,spx2), 7.01 MHz vs Method D using F(spx2,spx2), 7.10 MHz] instead of parabolic apodization [ie, Method B using F(plx2,spx2), 6.97 MHz vs Method A using F(spx2,spx2), 6.96 MHz]. In conjunction with this, the lateral frequencies became larger than when using the spherical waves, particularly when using rectangular apodization (ie, Method E with plx2 for tr, 2.89 MHz vs Method D with spx2 for tr, 2.16 MHz) rather than parabolic apodization (Method B with plx2 for tr, 3.12 MHz vs Method A with spx2 for tr, 2.92 MHz). As mentioned previously, this was due to the larger steering angles obtained using crossed plane waves (plx2) rather than crossed spherical waves (spx2). With respect to the apodizations for crossed plane waves, a rectangular apodization is not as effective for yielding large steering angles as parabolic apodization (the axial frequencies obtained using rectangular apodization are larger than those obtained using parabolic apodization). Thus, rectangular apodization is not suitable for such steered plane-wave transmissions (very low measurement accuracies are obtained). Compared with the cases using spx2 for tr, the small lateral bandwidths were also obtained for both the parabolic and rectangular apodizations (Methods A vs B and D vs E). Thus, disregarding lateral low-frequency spectra was not very effective for plx2 for tr (see the "LM and quasi-LM imaging" subsection and the "Measurements using LM and quasi-LM" subsection).

LM and quasi-LM imaging

Figure 6 shows B-mode images obtained with beamforming Methods A to J with a low lateral cutoff frequency f_c ranging from 0 to 4.63 MHz (original LMs using crossed wave transmissions, ie, Methods A, B, D, and E), 0 to 3.46 MHz (original LMs with a non-steered single plane-wave transmission, ie, Methods C and F) and 0 to 2.29 MHz (quasi-LMs, ie, Methods G to J). For B-mode imaging, the cosine LM was used. For the original LMs (Methods A to F),
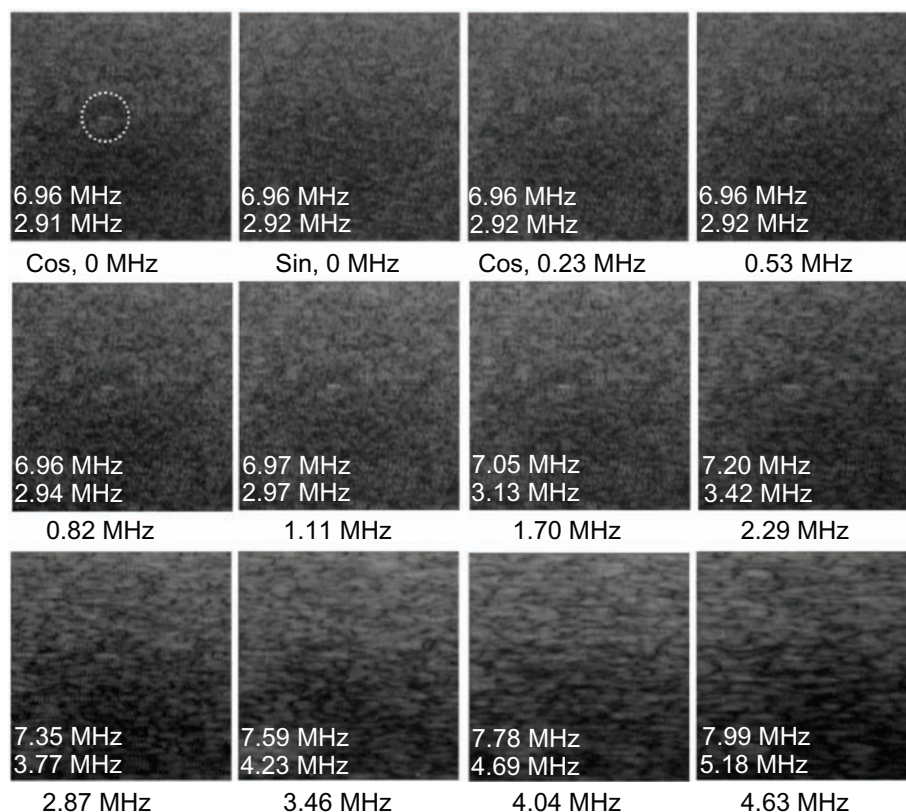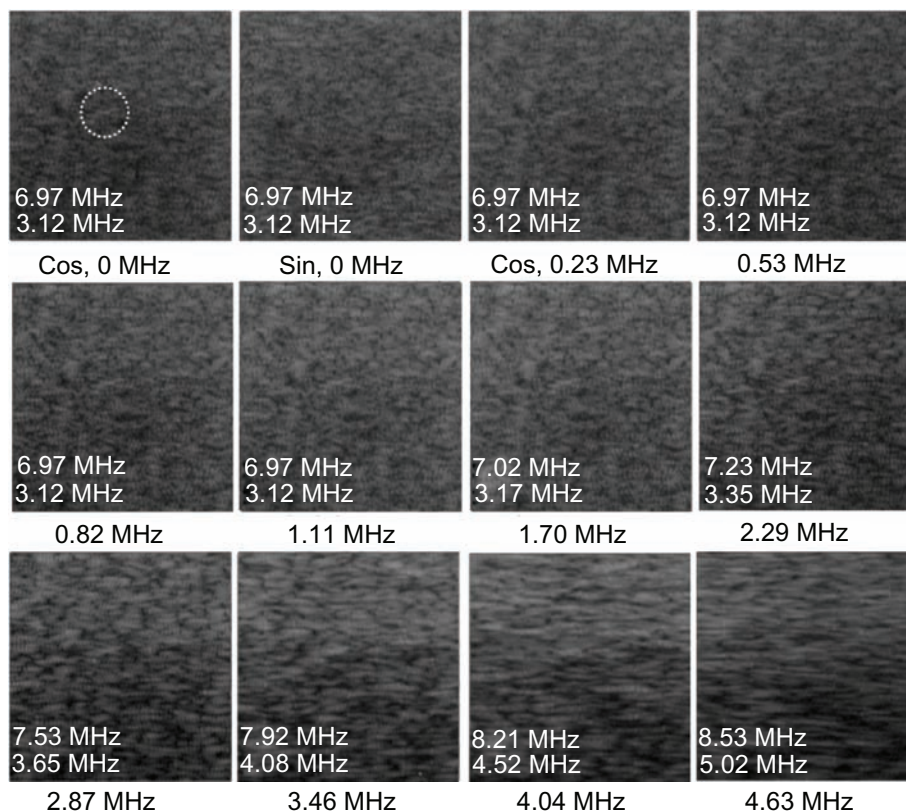
A Method A: F(sp×2; sp×2), A(tr,re)

6.96 MHz 2.91 MHz	6.96 MHz 2.92 MHz	6.96 MHz 2.92 MHz	6.96 MHz 2.92 MHz
Cos, 0 MHz	Sin, 0 MHz	Cos, 0.23 MHz	0.53 MHz
6.96 MHz 2.94 MHz	6.97 MHz 2.97 MHz	7.05 MHz 3.13 MHz	7.20 MHz 3.42 MHz
0.82 MHz	1.11 MHz	1.70 MHz	2.29 MHz
7.35 MHz 3.77 MHz	7.59 MHz 4.23 MHz	7.78 MHz 4.69 MHz	7.99 MHz 5.18 MHz
2.87 MHz	3.46 MHz	4.04 MHz	4.63 MHz

B Method B: F(pl×2; sp×2), A(re)

6.97 MHz 3.12 MHz	6.97 MHz 3.12 MHz	6.97 MHz 3.12 MHz	6.97 MHz 3.12 MHz
Cos, 0 MHz	Sin, 0 MHz	Cos, 0.23 MHz	0.53 MHz
6.97 MHz 3.12 MHz	6.97 MHz 3.12 MHz	7.02 MHz 3.17 MHz	7.23 MHz 3.35 MHz
0.82 MHz	1.11 MHz	1.70 MHz	2.29 MHz
7.53 MHz 3.65 MHz	7.92 MHz 4.08 MHz	8.21 MHz 4.52 MHz	8.53 MHz 5.02 MHz
2.87 MHz	3.46 MHz	4.04 MHz	4.63 MHz

Figure 6 (*Continued*)

C Method C: F(plx1; spx2), A(re)

7.16 MHz 1.55 MHz	7.16 MHz 1.55 MHz	7.16 MHz 1.56 MHz	7.18 MHz 1.60 MHz
Cos, 0 MHz	Sin, 0 MHz	Cos, 0.23 MHz	0.53 MHz

7.24 MHz 1.70 MHz	7.31 MHz 1.84 MHz	7.60 MHz 2.22 MHz	8.09 MHz 2.67 MHz
0.82 MHz	1.11 MHz	1.70 MHz	2.29 MHz

8.44 MHz 3.19 MHz	8.45 MHz 3.95 MHz
2.87 MHz	3.46 MHz

D Method D: F(spx2; spx2), A(-)

7.10 MHz 2.15 MHz	7.10 MHz 2.16 MHz	7.10 MHz 2.26 MHz	7.11 MHz 2.39 MHz
Cos, 0 MHz	Sin, 0 MHz	Cos, 0.23 MHz	0.53 MHz

7.10 MHz 2.58 MHz	7.10 MHz 2.78 MHz	7.07 MHz 3.26 MHz	7.08 MHz 3.69 MHz
0.82 MHz	1.11 MHz	1.70 MHz	2.29 MHz

7.07 MHz 4.11 MHz	7.13 MHz 4.58 MHz	7.23 MHz 5.03 MHz	7.39 MHz 5.48 MHz
2.87 MHz	3.46 MHz	4.04 MHz	4.63 MHz

Figure 6 (*Continued*)

E Method E: F(pl×2; sp×2), A(-)

7.01 MHz 2.88 MHz	7.01 MHz 2.89 MHz	7.04 MHz 2.95 MHz	7.01 MHz 2.91 MHz
Cos, 0 MHz	Sin, 0 MHz	Cos, 0.23 MHz	0.53 MHz
7.02 MHz 2.93 MHz	7.02 MHz 2.96 MHz	7.12 MHz 3.08 MHz	7.32 MHz 3.37 MHz
0.82 MHz	1.11 MHz	1.70 MHz	2.29 MHz
7.46 MHz 3.77 MHz	7.66 MHz 4.23 MHz	7.88 MHz 4.67 MHz	8.15 MHz 5.13 MHz
2.87 MHz	3.46 MHz	4.04 MHz	4.63 MHz

F Method F: F(pl×1; sp×2), A(-)

7.16 MHz 1.43 MHz	7.16 MHz 1.45 MHz	7.17 MHz 1.53 MHz	7.20 MHz 1.65 MHz
Cos, 0 MHz	Sin, 0 MHz	Cos, 0.23 MHz	0.53 MHz
7.22 MHz 1.84 MHz	7.22 MHz 2.03 MHz	7.35 MHz 2.41 MHz	7.70 MHz 2.83 MHz
0.82 MHz	1.11 MHz	1.70 MHz	2.29 MHz
8.08 MHz 3.29 MHz	8.26 MHz 3.89 MHz		
2.87 MHz	3.46 MHz		

Figure 6 (*Continued*)

G Method G: F(sp×1; sp×1), A(tr,re)

7.38 MHz 0.82 MHz	7.39 MHz 0.84 MHz	7.43 MHz 0.95 MHz	7.53 MHz 1.11 MHz
Cos, 0 MHz	Sin, 0 MHz	Cos, 0.23 MHz	0.53 MHz
7.65 MHz 1.35 MHz	7.78 MHz 1.59 MHz	7.92 MHz 1.87 MHz	8.07 MHz 2.13 MHz
0.82 MHz	1.11 MHz	1.41 MHz	1.70 MHz
8.26 MHz 2.40 MHz	8.40 MHz 2.71 MHz		
1.99 MHz	2.29 MHz		

H Method H: F(pl×1; sp×1), A(re)

7.32 MHz 0.55 MHz	7.33 MHz 0.57 MHz	7.42 MHz 0.68 MHz	7.65 MHz 0.86 MHz
Cos, 0 MHz	Sin, 0 MHz	Cos, 0.23 MHz	0.53 MHz
7.95 MHz 1.11 MHz	8.22 MHz 1.39 MHz	8.35 MHz 1.73 MHz	8.22 MHz 2.20 MHz
0.82 MHz	1.11 MHz	1.41 MHz	1.70 MHz
7.95 MHz 2.82 MHz	7.61 MHz 3.41 MHz		
1.99 MHz	2.29 MHz		

Figure 6 (*Continued*)

I Method I: F(sp×1; sp×1), A(-)

7.28 MHz 1.42 MHz	7.28 MHz 1.44 MHz	7.30 MHz 1.53 MHz	7.33 MHz 1.68 MHz
Cos, 0 MHz	Sin, 0 MHz	Cos, 0.23 MHz	0.53 MHz

7.36 MHz 1.88 MHz	7.38 MHz 2.07 MHz	7.42 MHz 2.28 MHz	7.52 MHz 2.47 MHz
0.82 MHz	1.11 MHz	1.41 MHz	1.70 MHz

7.66 MHz 2.67 MHz	7.83 MHz 2.90 MHz
1.99 MHz	2.29 MHz

J Method J: F(pl×1; sp×1), A(-)

7.32 MHz 0.81 MHz	7.32 MHz 0.82 MHz	7.37 MHz 0.92 MHz	7.48 MHz 1.06 MHz
Cos, 0 MHz	Sin, 0 MHz	Cos, 0.23 MHz	0.53 MHz

7.68 MHz 1.26 MHz	7.93 MHz 1.49 MHz	8.12 MHz 1.78 MHz	8.14 MHz 2.14 MHz
0.82 MHz	1.11 MHz	1.41 MHz	1.70 MHz

8.06 MHz 2.53 MHz	7.90 MHz 2.95 MHz
1.99 MHz	2.29 MHz

Figure 6 B-mode images versus low lateral cutoff frequency for spectra (Figure 4) obtained using beamforming Methods A to J as summarized in Table 1.
Note: Generated depth and lateral frequencies are depicted in the respective images.
Abbreviations: tr, transmission; re, reception; sp, spherical focusing using spherical waves; pl, non-focusing using plane waves; ×1 and ×2, non-crossed single and two crossed waves, respectively; F(tr,re), focusing using sp or non-focusing using pl for tr and re; A(tr and/or re), parabolic apodization for tr and/or re; A(non-described tr or re, or described as –): non-parabolic apodization using a rectangular window for tr or re, or both tr and re (ie, rectangular apodization or no apodization).

coherent superposition was performed. In the B-mode images, the intense scattering waves are circled for $f_c = 0$ MHz. As mentioned previously, the same scattering signals obtained using parabolic apodization are also circled in figure 7 in Sumi et al[15] and were obtained by the incoherent superposition of crossed beams. The effectiveness of the incoherent superposition (ie, the visualization of intense scattering) can also be confirmed by comparing the corresponding B-mode images [Method A with F(spx2; spx2) and A(tr,re), figure 7A in Sumi et al[15] vs Figure 6A; Method B with F(plx1; spx2) and A(re), figure 7B in Sumi et al[15] vs Figure 6B]. In the respective images (Figure 6A–J), the obtained axial and lateral frequencies are depicted. As shown, as the cutoff frequency f_c increases, the generated axial and lateral frequencies change; that is, increasing f_c increases the lateral frequencies. Interestingly, for the high lateral spatial resolution images originally obtained using rectangular apodization (Methods D, F, and I, etc), the intense scattering can be more clearly seen with increasing f_c (not circled), even though coherent superposition was performed. Such imaging can also be performed with incoherent superposition and will be reported in detail elsewhere.

For the low lateral cutoff frequency $f_c = 0$ MHz, the lateral oscillations can be confirmed for Methods A to C (ie, original LMs with parabolic apodization). As expected, for Methods D to F (ie, original LMs with rectangular apodization), such oscillations cannot be confirmed (this is because a lateral DC and very low lateral frequency spectra were also generated, as mentioned), although a high lateral spatial resolution due to rectangular apodization can be confirmed (large lateral bandwidths were obtained). When using the crossed plane-wave transmissions (ie, Methods B and E with plx2), the crossing of two steered plane waves can be confirmed and, obviously, the lateral frequencies and lateral bandwidths are respectively larger and smaller than those obtained using crossed spherical-wave transmissions with the same apodization functions (ie, Methods A and D with spx2). When using non-steered single plane waves (ie, Methods C and F with plx1), the lateral frequencies and lateral bandwidths are smaller than other wave transmissions. Further, for Methods G to J, using a single-beam scan with no steering, such lateral oscillations cannot be obtained. Method I with rectangular apodization also yields a high lateral resolution (a large lateral bandwidth). For all the respective focusing methods, rectangular apodization yields higher axial spatial resolutions than parabolic apodization (ie, larger axial bandwidths).

For comparison, B-mode images obtained with sine LM are also shown only for $f_c = 0$ MHz. The differences in cosine

and sine LM images can be clearly confirmed, for instance, from the intense scattering waves respectively visualized using $f_c = 0$ MHz (the cosine LM waves are circled). As expected, the sine LM yielded higher lateral frequencies than the cosine LM for Methods D to F (original LMs with rectangular apodization; eg, for Method D, 2.16 vs 2.15 MHz; Method F, 1.45 vs 1.43 MHz) and G to J (non-steered cases, ie, Method G, 0.84 vs 0.82 MHz; Method H, 0.57 vs 0.55 MHz; Method I, 1.44 vs 1.42 MHz; Method J, 0.82 vs 0.81 MHz) but not for Methods A to C – that is, original LMs with parabolic apodization, which did not generate a lateral DC or very low lateral frequency spectra. Only for such very small cutoff frequencies were the differences in the generated lateral frequencies notable, particularly for the non-steered cases and the original LMs with large lateral bandwidths (rectangular apodization), rather than for the original LMs with small lateral bandwidths (parabolic apodization).

Figure 7 depicts Methods A to J with respective sine and cosine LMs, and 7A shows the low lateral cutoff frequency f_c versus the axial frequencies for the original LMs and quasi-LMs (ie, for non-steered cases); 7B shows the low lateral cutoff frequency f_c versus the lateral frequencies for the original LMs; and 7C shows the low lateral cutoff frequency f_c versus the lateral frequencies for quasi-LMs. As shown, all the lateral frequencies monotonically increase (up to about 3.6 to 5.4 MHz for the original LMs; up to about 2.4 to 3.6 MHz for the quasi-LMs). However, for the cutoff frequency range with respect to Methods A, B, D, and E, the axial frequencies monotonically increase (up to about 7.4 to 8.5 MHz) and this happens over the same range with the other Methods (ie, Methods C, F, and G to J). The axial frequencies reach their respective maxima (up to about 8.1 to 8.6 MHz) before decreasing (over about 1.5 MHz). The quasi-LMs generate peaks of axial frequencies with smaller f_c values than the original LMs. The effects of disregarding low lateral frequency spectra can also be confirmed in the B-mode images. Although the lateral frequencies increase, absolutely the lateral spatial resolutions (lateral bandwidths) decrease. With respect to spatial resolution, disregarding low-frequency spectra is counterproductive except for yielding the increase in a lateral frequency (Methods A to F) and the quasi-LM imaging (Methods G to J). In general, envelope detection, not square detection, is used for B-mode imaging. Although square detection, as performed in this report, permits the visualization of wave oscillations, in the control using the cutoff frequency f_c, which cannot be achieved using envelope detection. This will be considered in the Discussion section.
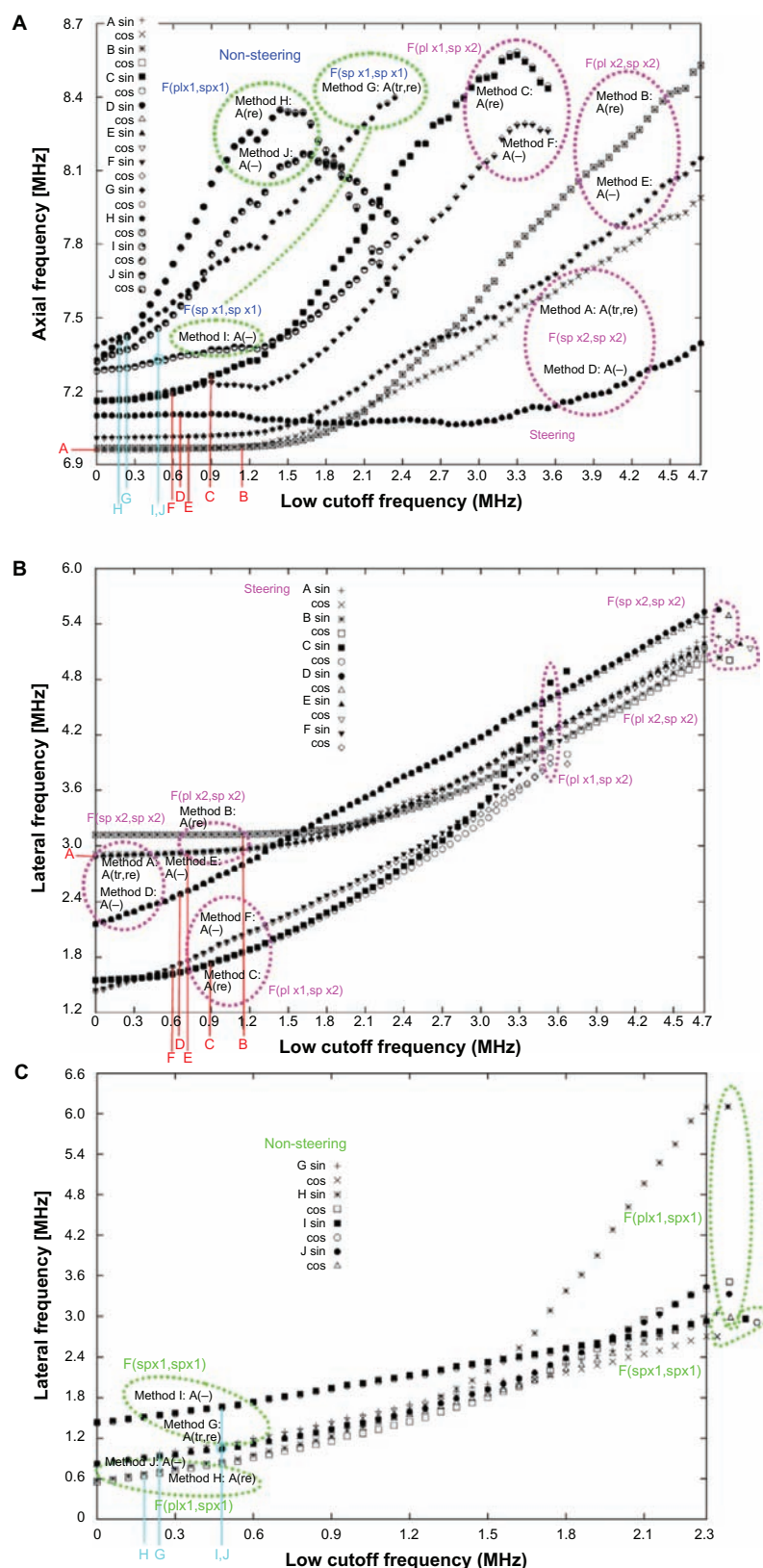
Figure 7 Frequencies generated versus low lateral cutoff frequency for spectra (Figure 4) obtained using beamforming Methods A to J as summarized in Table 1: (**A**) depth frequency, and lateral frequencies of (**B**) steered cases and (**C**) non-steered cases.

Note: In the figures, the low lateral cutoff frequencies that yielded the most accurate shear moduli measurements (Figure 10K and L) are shown.

Abbreviations: tr, transmission; re, reception; sp, spherical focusing using spherical waves; pl, non-focusing using plane waves; x1 and x2, non-crossed single and two crossed waves, respectively; F(tr,re), focusing using sp or non-focusing using pl for tr and re; A(tr and/or re), parabolic apodization for tr and/or re; A(non-described tr or re, or described as –): non-parabolic apodization using a rectangular window for tr or re, or both tr and re (ie, rectangular apodization or no apodization).

For Methods A to J, the correspondingly evaluated lateral autocorrelation functions (PSFs) at a depth of 19.0 mm (the central depth of the ROI) are shown in Figure 8, with the varying low cutoff frequency f_c values in the same ranges as those in Figures 6 and 7. With respect to the spatial resolutions obtained, the effects of disregarding low lateral frequency spectra can be more simply confirmed. That is, as the lateral low cutoff frequency f_c increases, the generated lateral frequencies increase. The widths of the autocorrelation functions become slightly larger. The main lobes and side lobes become narrow, and the number of the side lobes increases. The magnitude of the side lobes also increases. Specifically, for the original LMs, using crossed plane-wave transmissions (Method B with parabolic apodization and Method E with rectangular apodization), more rapid oscillations and larger magnitudes of the side lobes are obtained than when using crossed spherical-wave transmissions (Methods A and D with the same apodization functions). When using a non-steered single plane-wave transmission (Method C with parabolic apodization and Method F with rectangular apodization), although slower oscillations (lower frequencies) are obtained than when using crossed spherical-wave transmissions (Methods A and D with the same apodization functions), much larger magnitudes are obtained for the side lobes. For the quasi-LMs obtained from non-steered cases, as designed, almost the same widths are obtained for the autocorrelation functions (Methods G to J) as with the original LMs with the same apodization functions (Methods A, C, D and F). However, much slower oscillations are also obtained than with the original LMs. For the quasi-LMs, when using non-steered single plane-wave transmissions (Method H with parabolic apodization and Method J with rectangular apodization), although slower oscillations (lower frequencies) are obtained than when using spherical-wave transmissions (Methods G and I with the respective same apodization functions), much larger magnitudes are obtained for the side lobes. For the respective focusing methods (combinations of spx2, spx1, plx2, and plx1 for tr and re), when using rectangular apodization, the widths of the autocorrelation functions are smaller than those obtained with parabolic apodization. Moreover, the magnitudes of the side lobes are smaller than those obtained using parabolic apodization. For all of the beamforming methods, low frequencies or large magnitudes for the side lobes decrease the accuracy of displacement measurements and the quality of B-mode imaging (due to a decrease in the ability to visualize the distribution of scattering properties with high spatial resolution), except for permitting the visualization of intense scattering

waves originally obtained with a high spatial resolution, as mentioned.

Disregarding the low-frequency spectra is also beneficial for accurate measurements of a displacement vector and so forth (see the "Measurements using LM and quasi-LM" subsection). The cutoff frequencies that yielded the most accurate shear modulus measurements are depicted in Figure 7. For Methods A to J, accurate measurements of the shear modulus (shown in Figures 10 and 11) were obtained using rather small values of f_c (0 MHz or 0.55 to 1.2 MHz). Specifically, for Method A, disregarding the low-frequency spectra was counterproductive. Such small cutoff frequencies were also obtained for the quasi-LM cases (about 0.15 to 0.5 MHz). For all the measurements, sine LMs were used.

Measurements using LM and quasi-LM

As depicted in Figure 7, for the most accurate measurements achieved with the original LMs (Methods A to F), except for Methods A, B, D, and E, the notably increased axial frequencies were used (Methods C and F); except for Methods A and B, the notably increased lateral frequencies were also used (Methods C to F). For quasi-LMs (Methods G to J), the notably increased axial and lateral frequencies were used for all methods to obtain the most accurate measurements. The corresponding autocorrelation functions (PSFs) evaluated at a depth of 19.0 mm are shown in Figure 9 (9A, Methods A and D using spx2 for tr; 9B, Methods B and E using plx2 for tr; 9C, Methods C and F using plx1 for tr; 9D, Methods G and I using spx1 for tr; 9E, Methods H and J using plx1 for tr) (note that although the sine LMs were performed, theoretically, zero crossing at laterally central positions is not generated in the autocorrelation functions). In the figures, the optimal low lateral cutoff frequencies and the corresponding generated lateral frequencies are depicted. Note that although the lateral frequencies increase with an optimal f_c (eg, for Method D [Figure 9A], from 2.16 to 2.49 MHz; for Method I [Figure 9D], from 1.44 to 1.67 MHz), large magnitudes in the side lobes are not generated (large oscillations obtained with larger f_c are shown in Figure 8). However, also note that when using rectangular apodization, although Method E using crossed plane waves (Figure 9B) seems to have yielded better autocorrelation functions with oscillations (2.89 and 2.93 MHz) than Method D using crossed spherical waves (Figure 9A, 2.16 and 2.49 MHz), the measurement accuracies obtained are significantly lower (shown below). Alternatively, although Method I using non-steered beamforming (Figure 9D) yielded a low lateral
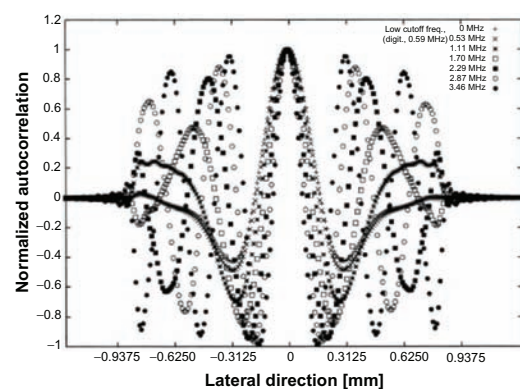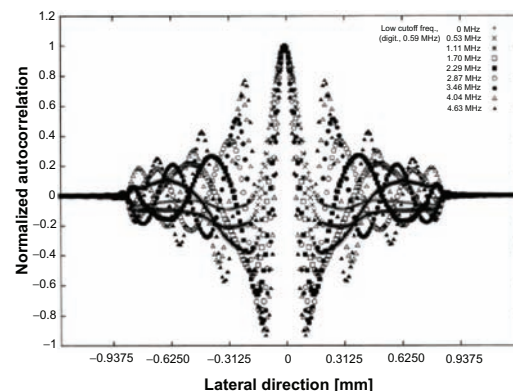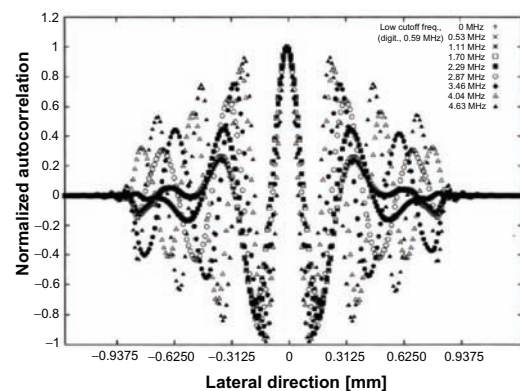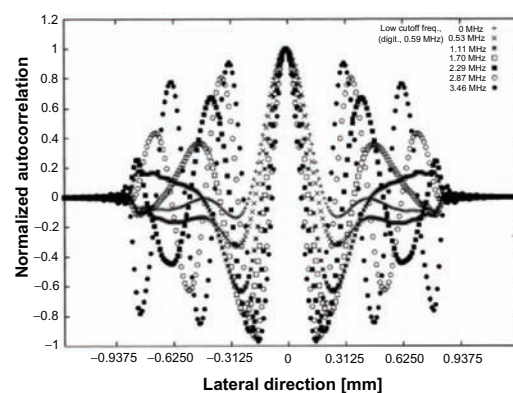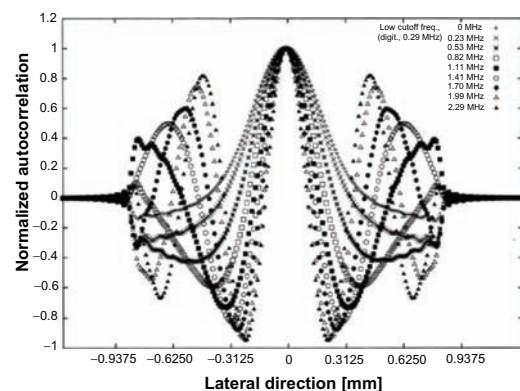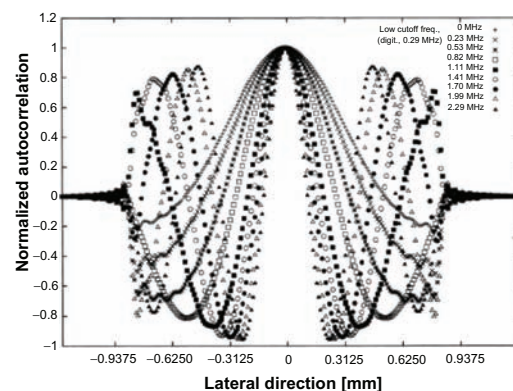
A Method A: F(spx2,spx2), A(tr,re)
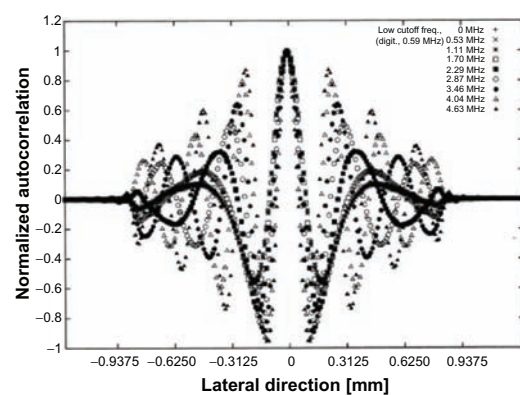
B Method B: F(plx2,spx2), A(re)
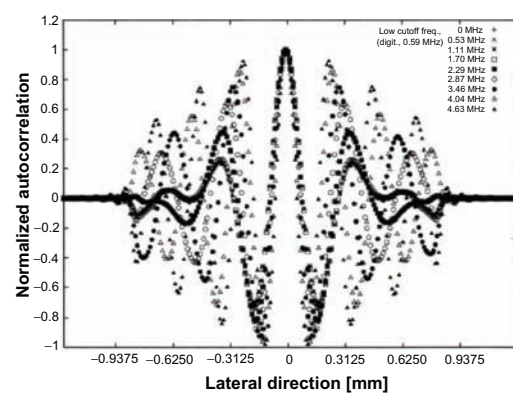
C Method C: F(plx1,spx2), A(re)

D Method D: F(spx2,spx2), A(-)

E Method E: F(plx2,spx2), A(-)

F Method F: F(plx1,spx2), A(-)

G Method G: F(spx1,spx1), A(tr,re)

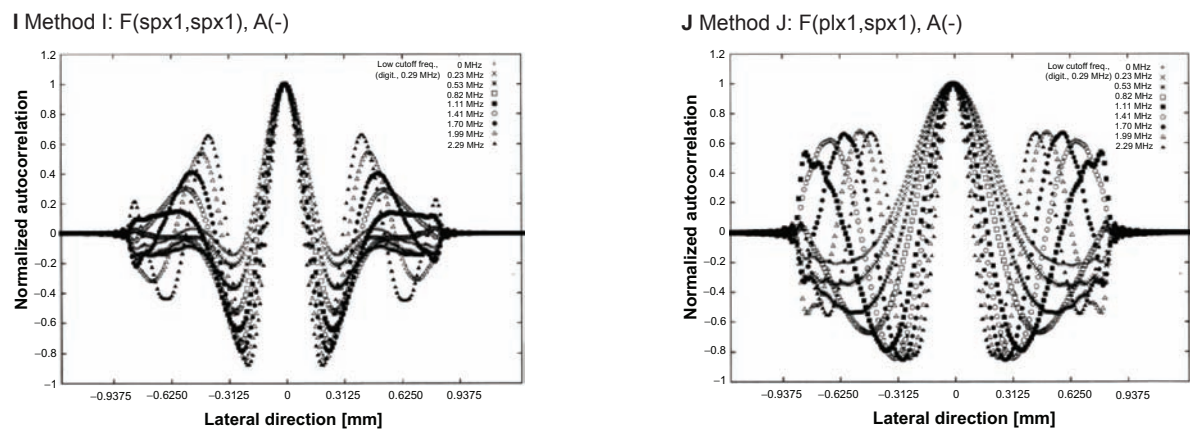**H** Method H: F(plx1,spx1), A(re)

Figure 8 (*Continued*)

I Method I: F(spx1,spx1), A(-)   **J** Method J: F(plx1,spx1), A(-)

Figure 8 Point spread functions generated versus low lateral cutoff frequency for spectra (Figures 4 and 7) obtained using beamforming Methods A to J as summarized in Table 1.
Abbreviations: tr, transmission; re, reception; sp, spherical focusing using spherical waves; pl, non-focusing using plane waves; x1 and x2, non-crossed single and two crossed waves, respectively; F(tr,re), focusing using sp or non-focusing using pl for tr and re; A(tr and/or re), parabolic apodization for tr and/or re; A(non-described tr or re, or described as −): non parabolic apodization using a rectangular window for tr or re, or both tr and re, ie, rectangular apodization or no apodization.

frequency even with additional processing (1.67 MHz), the measurement accuracy was significantly high. This is due to the respective low and high echo SNRs. Also note that for both Methods B and E, the differences cannot be confirmed visually in the raw and best autocorrelation functions (Figure 9B). This exhibits the high sensitivity of the cutoff frequency with respect to the measurement accuracy and the instability of the crossed plane waves (shown below).

Figure 10 shows statistics for Methods A to J, evaluated for their measurements of displacement vector magnitudes and angles; lateral, axial, and shear strains; and relative shear moduli obtained with the varying values of f_c shown in Figure 7. In the results regarding lateral (Figure 10E and F) and axial (Figure 10G and H) strains, and shear moduli (Figure 10K and L), the low lateral cutoff frequencies that yielded the most accurate shear moduli measurements are depicted. Specifically, the accurate means (Figure 10K) and small SDs (Figure 10L) of the shear moduli in the stiff inclusion are used as measures for determining the most accurate measurements. In Figure 11A–J, with the measurement results obtained with $f_c = 0$ MHz, the corresponding most accurate measurements of the displacement vector components, strain tensors, and shear moduli are imaged in gray scale. In Figure 11, the statistics evaluated in the stiff inclusion are depicted for lateral and axial strains, and shear moduli. The increase in measurement accuracy can be confirmed in Figure 10 and, visually, the improvement can also be confirmed in Figure 11.

Originally, the original LM with F(spx2,spx2) and A(tr,re) (ie, Method A) yielded the most accurate measurements (relative mean 3.27; SD 0.33, as depicted in Figure 11A) without any additional processing.[15] That is, for Method A, their accuracies were almost the same as those obtained

using cosine LM.[15] With Method A, fc is not used. For Method B using crossed plane waves [F(plx2,spx2)], the effect of the new SFDM can be confirmed (Figure 11B). The mean of the shear moduli becomes accurate (from 2.64 to 2.68) and the corresponding SD and those of the lateral and axial strains become smaller (eg, for lateral strain, from 17.53 to 16.35 × 10⁻³). However, fc is sensitive with respect to the measurement accuracy (Figure 10K and L). In addition, with Method C [F(plx1,spx2)], the proper use of f_c increases the accuracy of shear modulus measurements (from 4.59 to 3.80). However, the geometries of the stiff inclusion detected with use of Methods B and C are distorted (see Figure 11B and C). Also note that the use of crossed plane waves (Method B) yielded larger SDs than the use of a single plane wave (Method C), although more accurate measurements were obtained (Figure 10E–H). This was pronounced for the use of rectangular apodization as shown below (Methods E and F).

Examining the use of rectangular apodization (ie, no apodization) for the original LMs, Method D with F(spx2,spx2) yielded almost the same accuracy in measurements when using the proper f_c (0.64 MHz) as Method A, which obtained the most accurate measurements (Figure 11D). The mean shear modulus becomes accurate (from 3.54 to 3.28) and the SD becomes smaller (from 0.37 to 0.34). The geometry of the stiff inclusion is also circular. Although the increase in measurement accuracy is also confirmed for originally inaccurate Methods E and F (means of shear moduli from 1.50 to 2.64 and 1.83 to 3.45, respectively), the new SFDM was not very effective for the combination of plane-wave transmissions and rectangular apodization (see Figure 11E and F). Compared with the other beamforming methods, the measurement accuracies
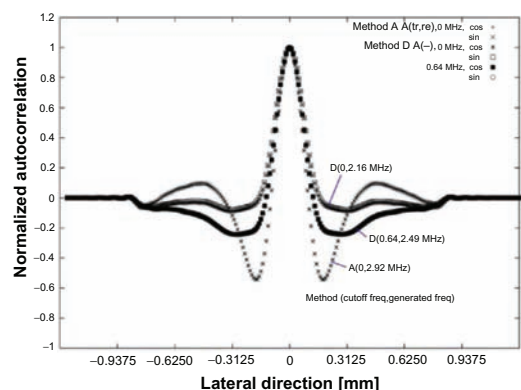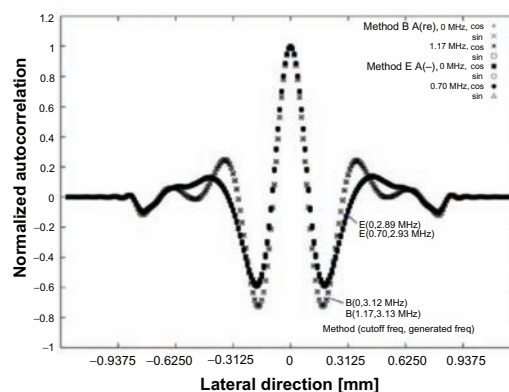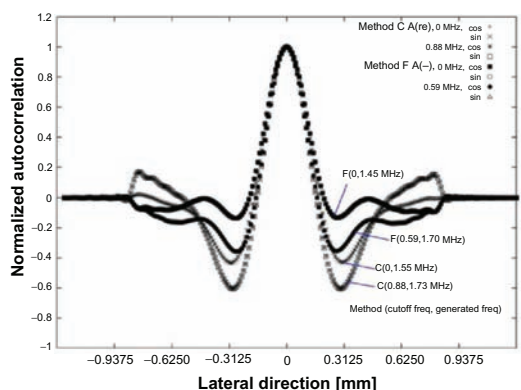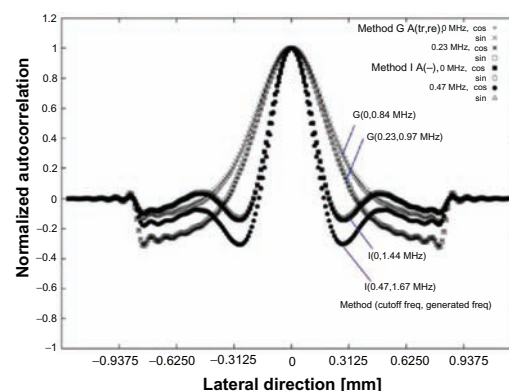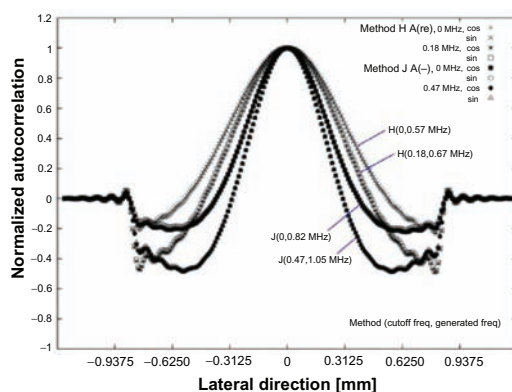
A Methods A and D, F(spx2, spx2)

B Methods B and E, F(plx2, spx2)

C Methods C and F, F(plx1, spx2)

D Methods G and I, F(spx1, spx1)

E Methods H and J, F(plx1, spx1)

Figure 9 Point spread functions obtained for original spectra (Figure 4) using beamforming Methods A to J (Table 1) and spectra with the low lateral cutoff frequencies that yielded the most accurate shear moduli measurements (Figure 10K and L).
Notes: Generated lateral frequencies are also depicted. Gray-scale images of the corresponding measurements of displacement vector components, strain tensor components, and shear moduli are shown in Figure 11.
Abbreviations: tr, transmission; re, reception; sp, spherical focusing using spherical waves; pl, non-focusing using plane waves; x1 and x2, non-crossed single and two crossed waves, respectively; F(tr,re), focusing using sp or non-focusing using pl for tr and re; A(tr and/or re), parabolic apodization for tr and/or re; A(non-described tr or re, or described as –): non parabolic apodization using a rectangular window for tr or re, or both tr and re, ie, rectangular apodization or no apodization.

are significantly lower even with the additional processing, particularly when performing a comparison between Methods E and D using steered beamforming. Inaccurate means and very large SDs (eg, lateral strains for Methods D, E, and F: 4.11 vs 49.10 vs 16.57 $\times$ 10^{-3}, respectively; axial strains,

13.39 vs 229.89 vs 44.18 $\times$ 10^{-4}, respectively) were obtained, and the geometry of the inclusion was distorted. This was due to a low-echo SNR. For Method E, the high sensitivity of fc with respect to a measurement accuracy was also confirmed (Figure 10K and L).

For quasi-LMs with parabolic (Figure 11G and H) and rectangular (Figure 11I and J) apodizations using optimal values of f_c, spherical-wave transmissions [Methods G and I with F(spx1,spx1)] were more effective than non-steered single plane-wave transmissions [Methods H and J with F(plx1,spx1)]. Because rectangular apodization (Method I) yielded a larger lateral bandwidth and a larger generated lateral frequency than parabolic apodization (Method G), the most accurate measurements were obtained and, specifically, the accuracy was almost the same as those of the most accurate measurements (Method A); that is, Method I, 3.27 and 0.32 (when f_c = 0 MHz, 3.59 and 0.37) vs Method G, 3.13 and 0.32 (when f_c = 0 MHz, 3.02 and 0.30) (see Figure 11G, I, and A). This was due to a high echo SNR obtained in the high-frequency range as well as in the disregarded low-frequency range. Although the effects of the new SFDMs were also confirmed for single non-steered plane-wave transmissions, the measurements were inaccurate and the geometry of the stiff inclusion was distorted (see means and SDs depicted in Figure 11H and J). Further, rectangular apodization (Figure 11J) yielded more accurate measurements than parabolic apodization (Figure 11H). Method I was the most stable of all the quasi-LM methods (Figure 10).

Speckle reduction

Incoherent superposition of horizontal, vertical, and simultaneous horizontal and vertical divisions of spectra were performed for beamforming Methods G and I (the corresponding spectra are shown in Figure 4G and I) – that is, using parabolic apodization for tr and re and no apodization (ie, rectangular apodization) with non-steered spherical focusing for tr and re, ie, F(spx1, spx1). Divided spectra were weighted so that the respective energies of the spectra become the same, and the incoherent signals were obtained using square detection. The respectively obtained images are shown in Figure 12A and B in a log-gray-scale. The rectangular image size is 19.7 (depth) × 20.7 (lateral) mm (depth 8.9 mm) centered on the ROI (13.2 × 13.7 mm). As shown for the respective apodizations, the number of divisions increased to up to eight for the respective directions, and the effects of speckle reduction increased. Simultaneously, the spatial resolution decreases in the same direction of decreasing bandwidth. Although the effects of speckle reduction were obtained for the respective divisions, the effects were the most intense for the simultaneous horizontal and vertical divisions. As a result, the existence of an inclusion can be clearly visualized. The fine images were obtained with rectangular
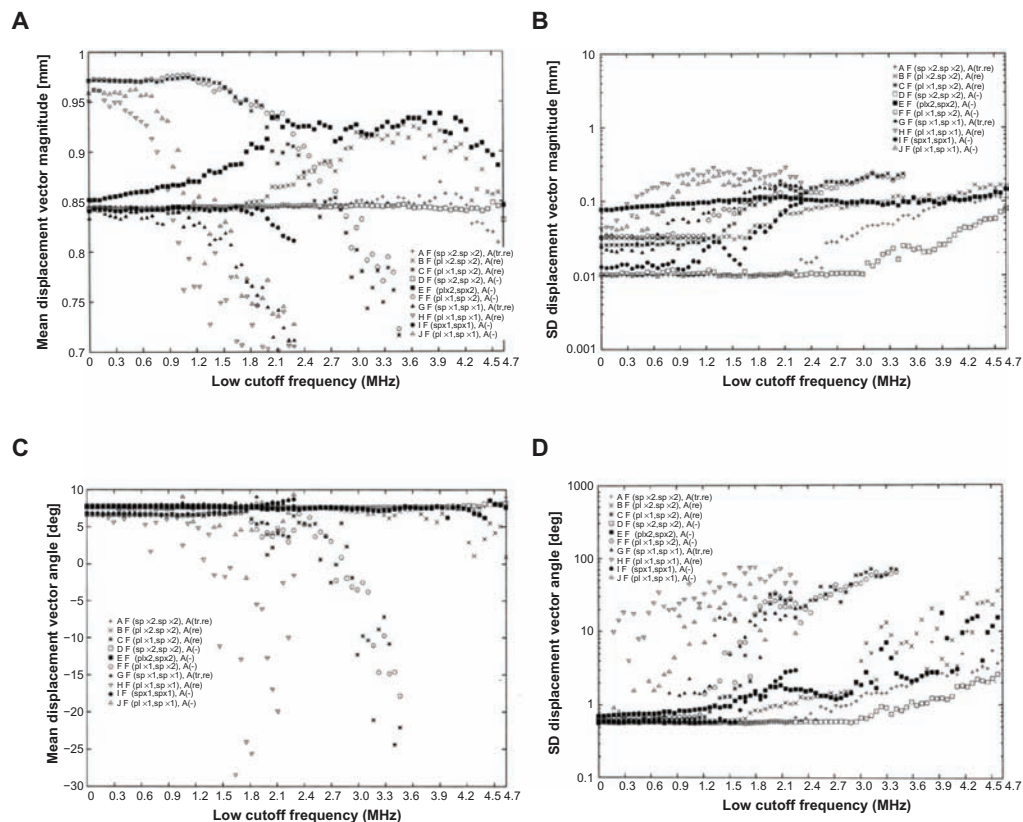
Figure 10 (*Continued*)
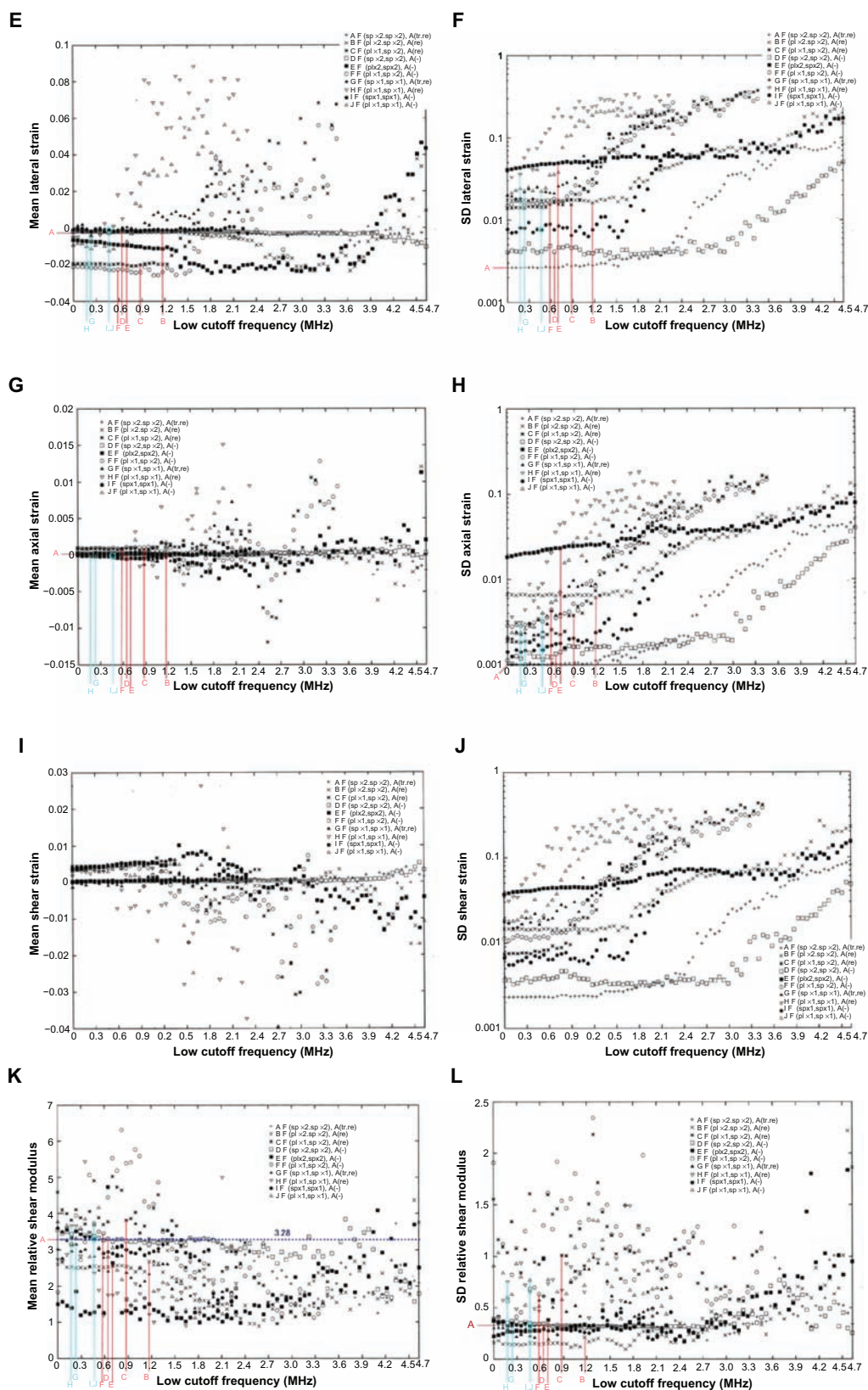
Figure 10 Statistics (means and standard deviations) obtained for displacement vector magnitudes and angles, lateral, axial and shear strains, and relative shear moduli obtained versus low lateral cutoff frequency for spectra (Figure 4) obtained by using beamforming Methods A to J as summarized in Table 1. For lateral (**E** and **F**) and axial (**G** and **H**) strains, and shear moduli (**K** and **L**), the low lateral cutoff frequencies that yielded the most accurate shear moduli measurements (**K** and **L**) are depicted.
Abbreviations: tr, transmission; re, reception; sp, spherical focusing using spherical waves; pl, non-focusing using plane waves; x1 and x2, non-crossed single and two crossed waves, respectively; F(tr,re), focusing using sp or non-focusing using pl for tr and re; A(tr and/or re), parabolic apodization for tr and/or re; A(non-described tr or re, or described as –): non parabolic apodization using a rectangular window for tr or re, or both tr and re, ie, rectangular apodization or no apodization.

apodization rather than with parabolic apodization due to the inherent high spatial resolution. The difference can be confirmed for the remaining speckle sizes and the boundary between the inclusion and the surrounding region. Also note that for these beamforming methods, the top and bottom boundaries are especially well visualized due to the horizontal division rather than the vertical

division (however, with a low spatial resolution). Further, the intense scattering signals circled in Figure 6 (B-mode images obtained through coherent superposition) are well visualized using a horizontal division rather than a vertical division (also with a low spatial resolution). Although such effects obtained with the horizontal division can also be obtained for simultaneous horizontal and vertical

A Method A: F(sp×2, sp×2), A(tr,re) [Parabolic LSM modulation = parabolic LCM]
LOW cutoff freq, 0 MHz; axial, 6.96 and lateral, 2.92 MHz
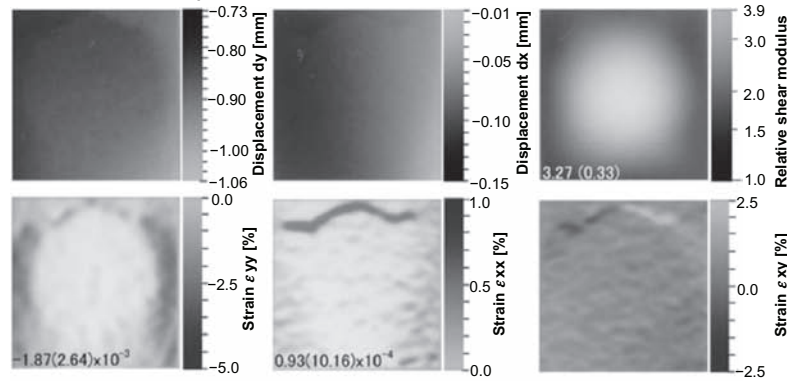
B Method B: F(pl×2, sp×2), A(re) [Parabolic LSM]
LOW cutoff freq, 0 MHz; axial, 6.97 and lateral, 3.12 MHz
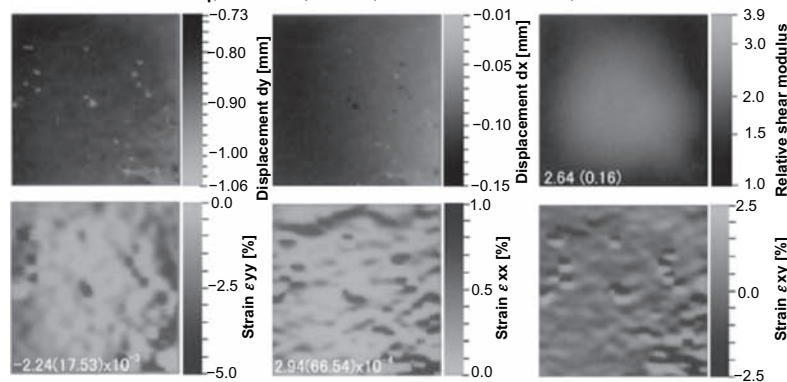
LOW cutoff freq, 1.17 MHz; axial, 6.97 and lateral, 3.13 MHz
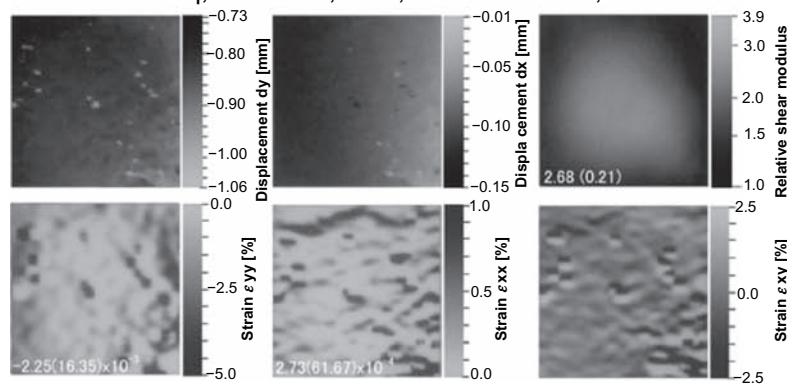
Figure 11 (*Continued*)

C Method C: F(pl×1, sp×2), A(re) [Parabolic LSM]
LOW cutoff freq, 0 MHz; axial, 7.16 and lateral, 1.55 MHz
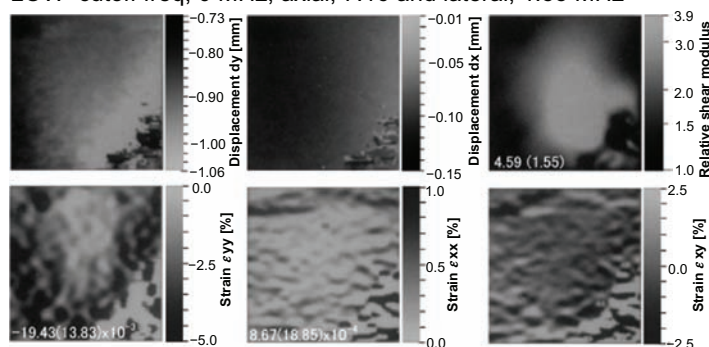
LOW cutoff freq, 0.88 MHz; axial, 7.26 and lateral, 1.73 MHz
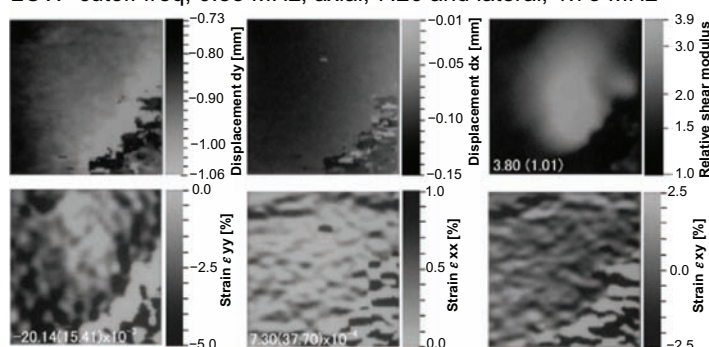
D Method D: F(spx2, sp×2), A(−) [Rectangular LSM]
LOW cutoff freq, 0 MHz; axial, 7.10 and lateral, 2.16 MHz
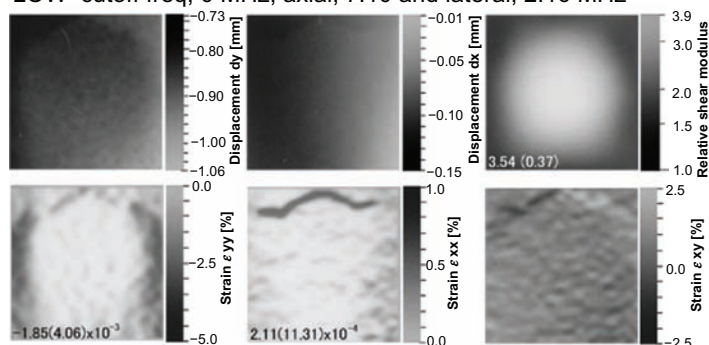
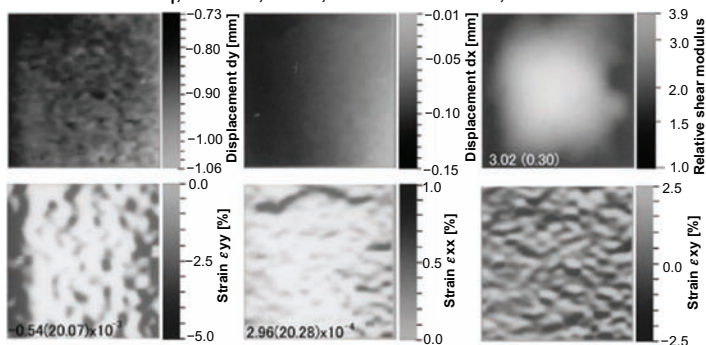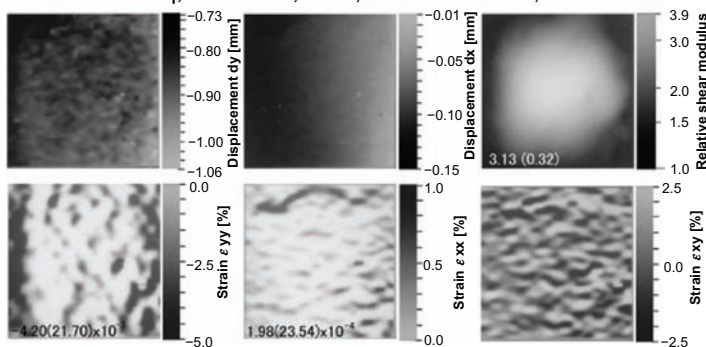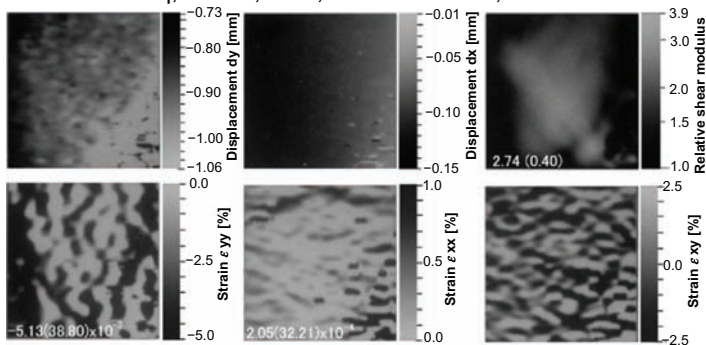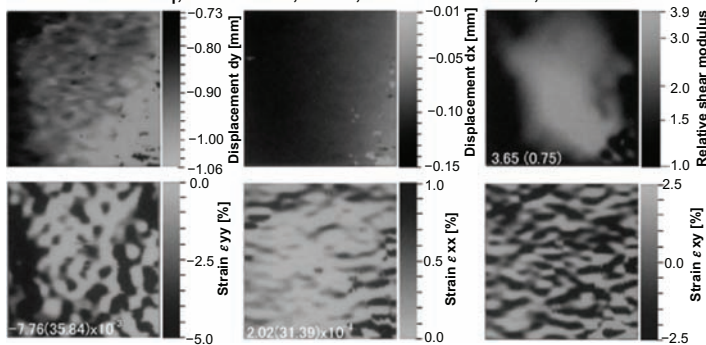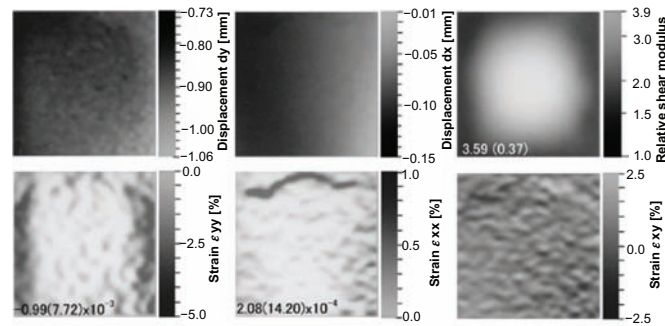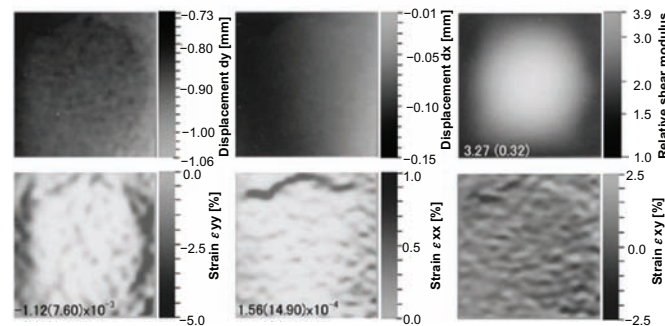Low cutoff freq, 0.64 MHz; axial, 7.11 and lateral, 2.49 MHz
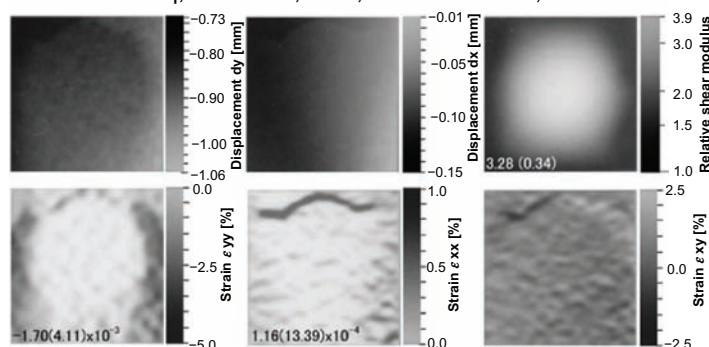
Figure 11 (*Continued*)

E Method E: F(pl×2, sp×2), A(−) [Rectangular LSM]
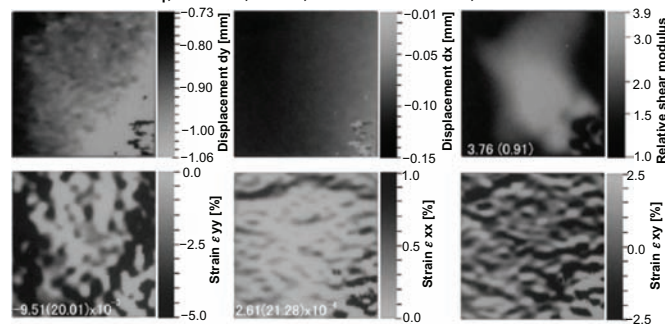Low cutoff freq, 0 MHz; axial, 7.01 and lateral, 2.89 MHz
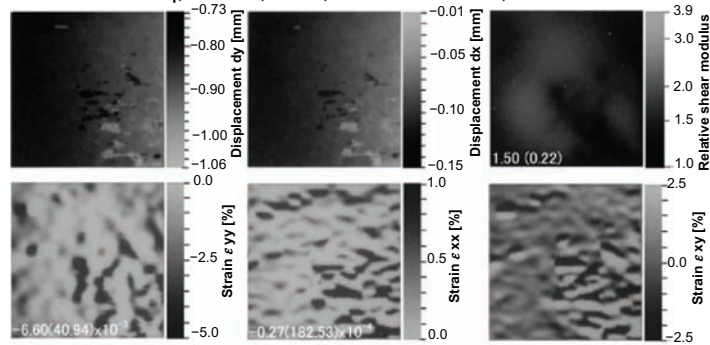
Low cutoff freq, 0.70 MHz; axial, 7.02 and lateral, 2.93 MHz
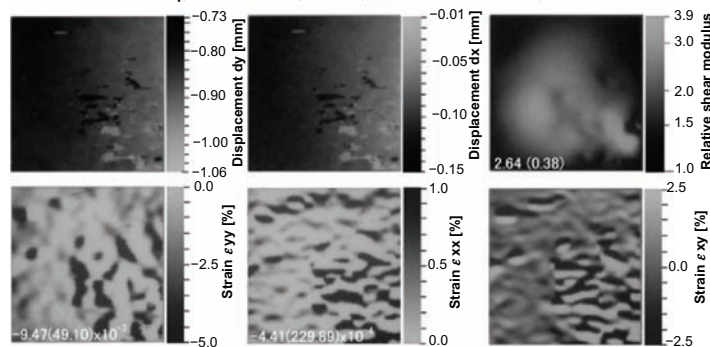
F Method F: F(pl×1, sp×2), A(−) [Rectangular LSM]
Low cutoff freq, 0 MHz; axial, 7.16 and lateral, 1.45 MHz
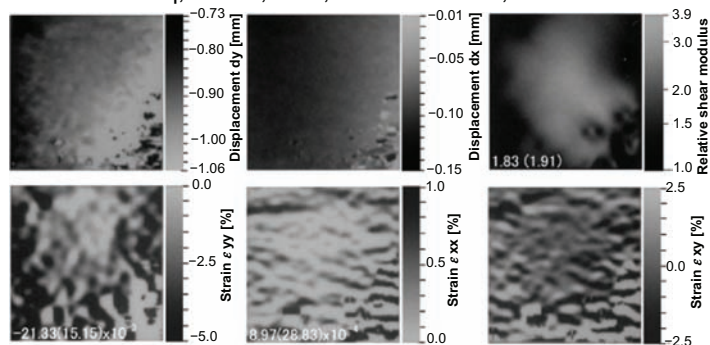
Low cutoff freq, 0.59 MHz; axial, 7.21 and lateral, 1.70 MHz
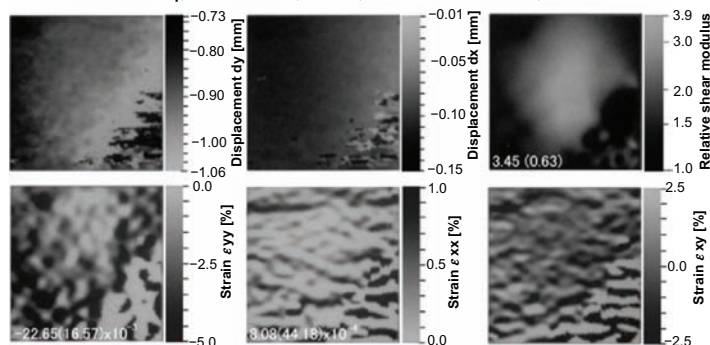
Figure 11 (*Continued*)

G F(sp×1, sp×1), A(tr,re) [Parabolic no LM]
Low cutoff freq, 0 MHz; axial, 7.39 and lateral, 0.84 MHz

Low cutoff freq, 0.23 MHz; axial, 7.43 and lateral, 0.97 MHz

H Method H: F(pl×1, sp×2), A(re) [Parabolic no LM]
Low cutoff freq, 0 MHz; axial, 7.33 and lateral, 0.57 MHz

Low cutoff freq, 0.18 MHz; axial, 7.40 and lateral, 0.67 MHz

Figure 11 (*Continued*)

I Method I: F(sp×1, spx1), A(-) [Rectangular no LM]
Low cutoff freq, 0 MHz; axial, 7.28 and lateral, 1.44 MHz

Low cutoff freq, 0.47 MHz; axial, 7.32 and lateral, 1.67 MHz

J Method J: F(pl×1, sp×1), A(-) [Rectangular no LM]
Low cutoff freq, 0 MHz; axial, 7.32 and lateral, 0.82 MHz

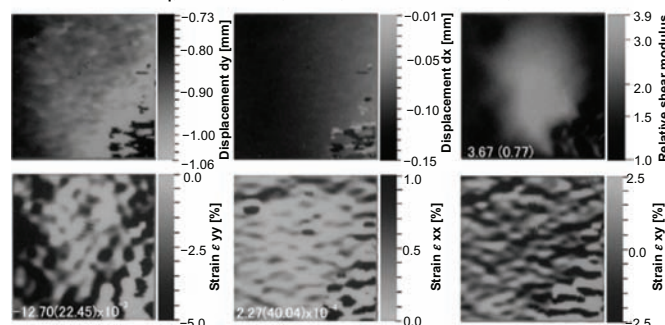Low cutoff freq, 0.47 MHz; axial, 7.46 and lateral, 1.05 MHz

Figure 11 Gray-scale images of measurements of axial and lateral displacement vector components, axial, lateral and shear strain tensor components, and shear moduli obtained for original spectra (Figure 4) with beamforming Methods A to J (Table 1) and spectra with the low lateral cutoff frequencies that yielded the most accurate shear moduli measurements (Figure 10K and L). The corresponding point spread functions are shown in Figure 9.
Abbreviations: LSM, lateral sine modulation; LCM, lateral cosine modulation; LM, lateral modulation; tr, transmission; re, reception; sp, spherical focus using spherical waves; pl, non-focused using plane waves; ×1 and ×2, non-crossed single and two crossed waves, respectively; F(tr,re), focused using sp or non-focus using pl for tr and re; A(tr and/or re), parabolic apodization for tr and/or re; A(non-described tr or re, or described as −): non parabolic apodization using a rectangular window for tr or re, or both tr and re, ie, rectangular apodization or no apodization.

divisions, simultaneous vertical division is beneficial for 2D speckle reduction (compare the results obtained using the simultaneous divisions with those obtained using the horizontal division alone).

To quantitatively evaluate the effects of speckle reduction using horizontal, vertical, and simultaneous horizontal and vertical divisions for the three cases, SD/mean was evaluated for the log scale data in the right three regions depicted in the raw B-mode images in Figure 12A and B (depths, 10.2 to 16.1, 16.1 to 22.0, and 22.0 to 27.9 mm), and the results are shown in Figure 13A to C. As shown, for all the divisions, as the number of divisions increases, SD/mean decreases. Further, note that the horizontal division is more effective for decreasing SD/mean than the vertical division (the respective

minima achieved by the horizontal and vertical divisions, about 0.3 vs about 0.4), and the simultaneous divisions yielded the smallest value of SD/mean (about 0.2). The effects of speckle reduction were larger for the deeper regions. For the horizontal division, in shallow regions, rectangular apodization is more effective for yielding a small value of SD/mean than parabolic apodization. For the other regions, the situation is vice versa. For the vertical and simultaneous divisions, when the number of divisions is small, parabolic apodization yields a smaller SD/mean than rectangular apodization, but when the number increases (>3), rectangular apodization provided more intense speckle reduction than parabolic apodization. For comparison, the results obtained using nondivided, original spectra and the divisions are also

A Method G: F(spx1, spx1), A(tr,re)
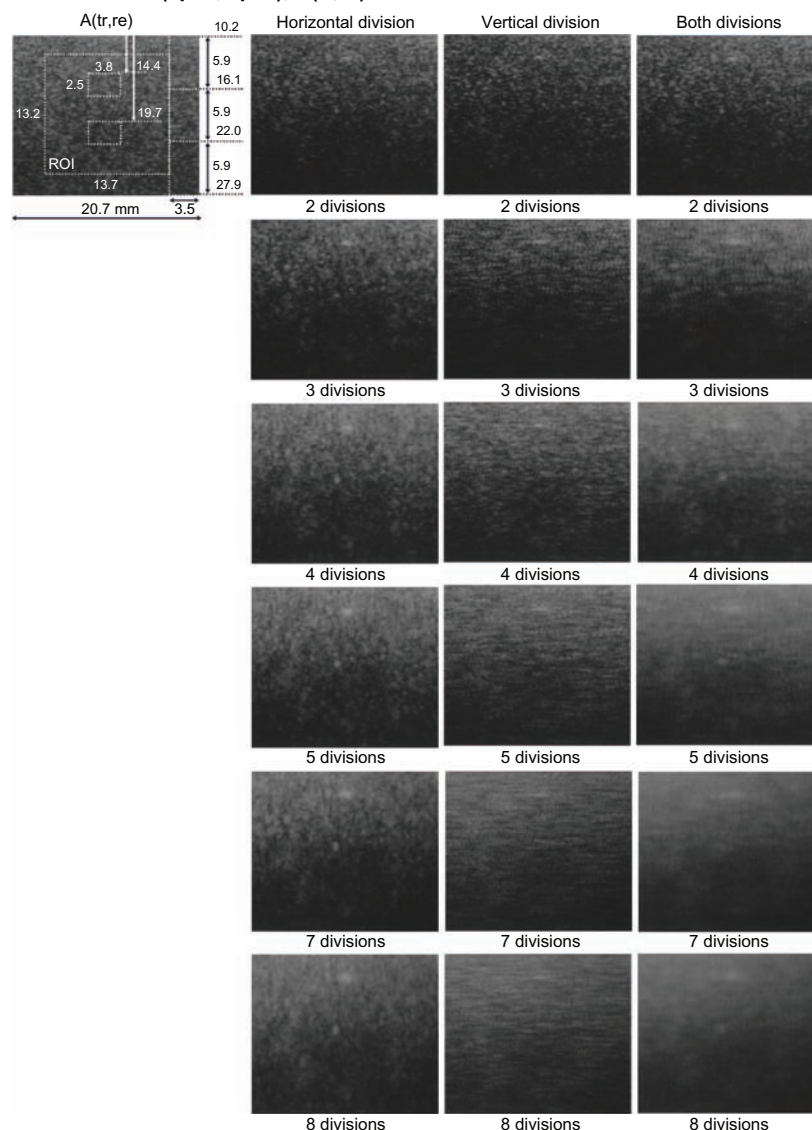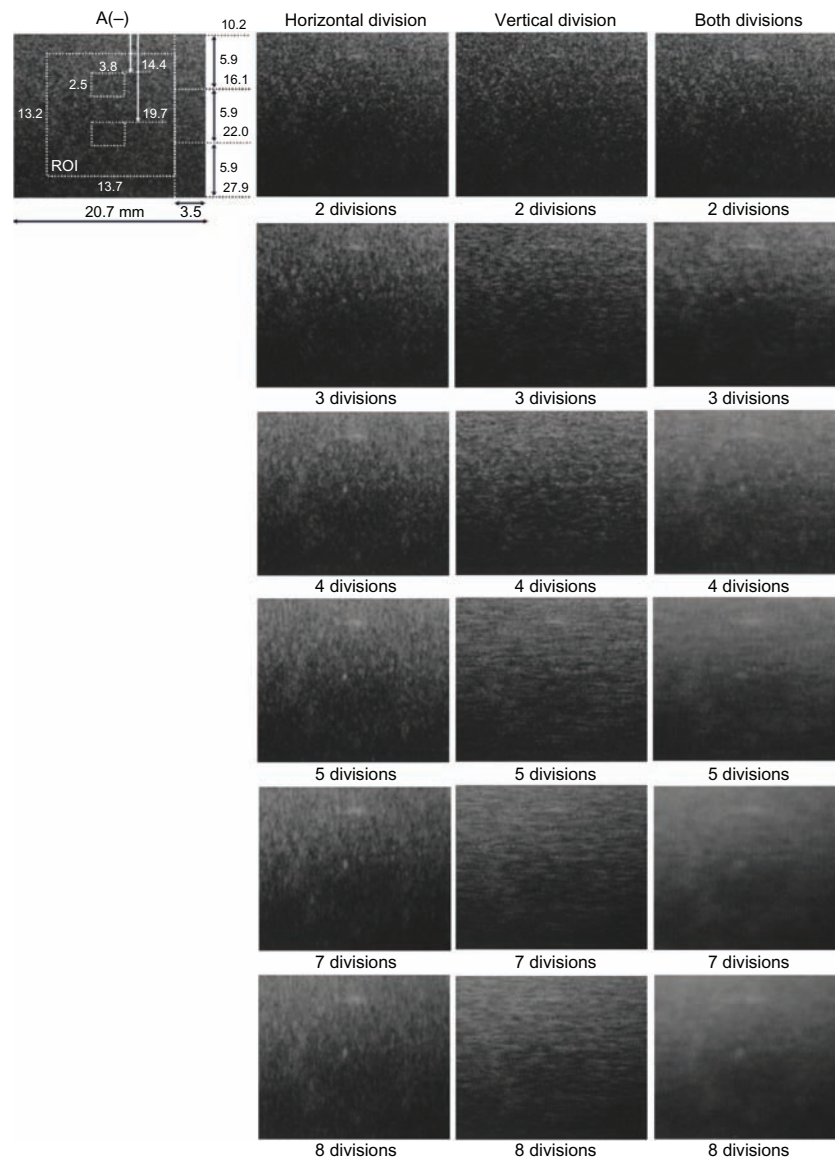
Figure 12 (*Continued*)

B Method I: F(spx1, spx1), A(–)

Figure 12 (**A**) B-mode images obtained through incoherent superposition of horizontal divisions, vertical divisions, and both divisions of spectra for beamforming with Methods G and I (the corresponding spectra are shown in Figure 4G and I): (**A**) using parabolic apodization for tr and re and (**B**) using non-parabolic apodization (ie, rectangular apodization) with non-steered spherical focusing for tr and re (ie, Focus(spx1,spx1).
Abbreviations: tr, transmission; re, reception; sp, spherical focusing using spherical waves; x1, non-crossed single waves; F(tr,re), spherical focusing for tr and re; A(tr,re), parabolic apodization for tr and re; and A(–), non-parabolic apodization using rectangular windows (ie, rectangular apodization or no apodization).

shown (the corresponding images are omitted). Because the results obtained are larger than those obtained without using the original spectra, the original echo data should not be used together with SFDM for speckle reduction.

The contrast-to-noise ratio (CNR) was also evaluated for the two regions depicted in the inclusion (Figures 12A and B; depths, 14.4 to 16.9 and 19.7 to 22.2 mm) with respect to the region surrounding the inclusion at the same depths:

$$CNR = \sqrt{\frac{2(M_I - M_S)^2}{V_I + V_S}} \qquad (13)$$

where M_I, M_S, V_I, and V_S are the means (M) and variances (V) of the log-scaled superposition of square-detected echo signals in the two regions in the inclusion (I) and in the regions surrounding the inclusion at the same depths (S).

As shown in Figure 14A to C, for all the divisions, large CNRs were obtained for the deeper region. Interestingly, for the horizontal division, except for the small number of divisions (<4) in the shallow region, parabolic apodization yielded larger CNRs than rectangular apodization. For the vertical and simultaneous divisions, the rectangular division
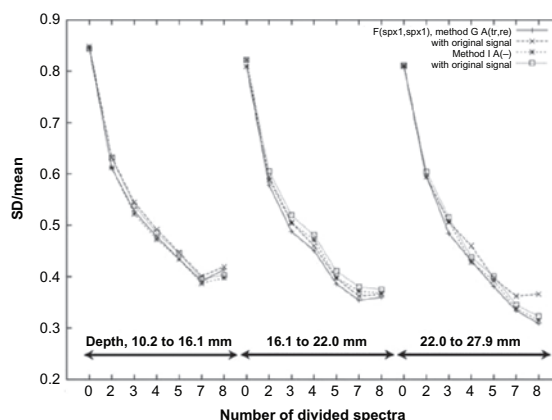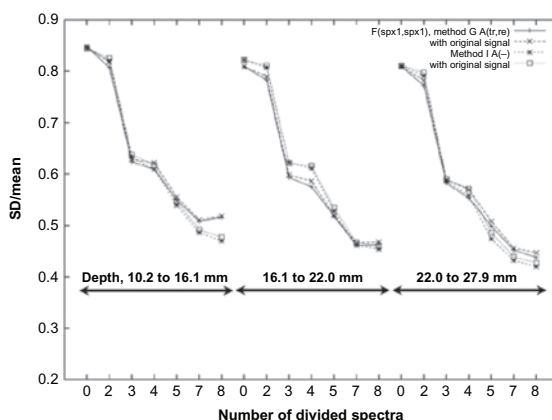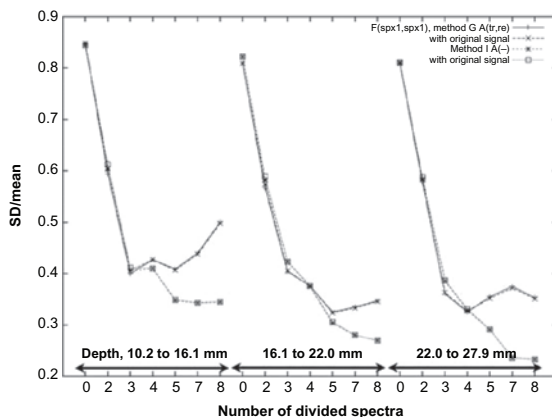
A Horizontal division

B Vertical division

C Both divisions

Figure 13 For incoherent superposition of horizontal divisions, vertical divisions, and both divisions for spectra with beamforming Methods G and I (the corresponding B-mode images shown in Figure 12A and B; the corresponding original spectra are shown in Figure 4G and I), the relative values for standard deviation/mean estimated on the B-mode images for the three right-side regions depicted in the original B-mode images shown in Figure 12A and B: (**A**) using parabolic apodization for tr and re and (**B**) using non-parabolic apodization (ie, rectangular apodization) with non-steered spherical focusing for tr and re – ie, Focus(spx1,spx1).
Abbreviations: tr, transmission; re, reception; sp, spherical focusing using spherical wave; x1, non-crossed single wave; F(tr,re), spherical focusing for tr and re; A(tr,re), parabolic apodization for tr and re; and A(−), non-parabolic apodization using rectangular windows (ie, rectangular apodization or no apodization).

yielded more large CNRs than parabolic apodization. The use of original echo signals (nondivided) was not effective in obtaining a large CNR.

Summarizing, for the non-steering case, 2D speckle reduction using the SFDM was more effective with rectangular apodization than with parabolic apodization, as expected.
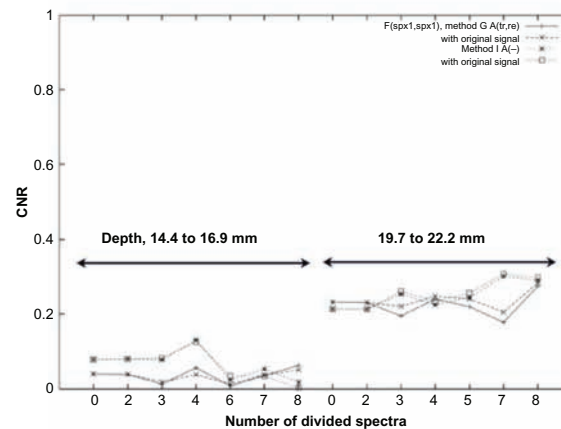
Discussion

In the agar phantom experiments (with a nominal US frequency of 7.5 MHz), the new SFDMs were able to improve both the original LMs using physically crossed, steered beams (Methods A to F) and single non-steered beams (ie, quasi-LMs using Methods G to J), using the new LM echo

A Horizontal division
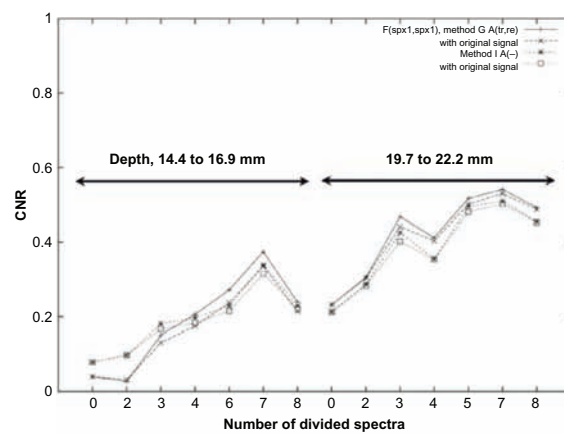
B Vertical division
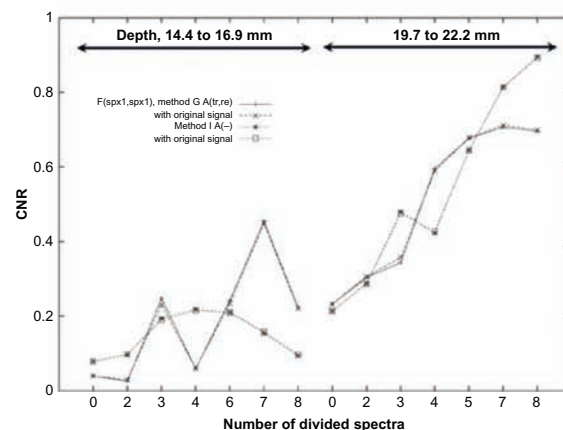

C Both divisions

Figure 14 For incoherent superposition of spectra, horizontal divisions, vertical divisions, and both divisions of spectra with beamforming Methods G and I are shown (the corresponding B-mode images are shown in Figure 12A and B; the corresponding original spectra are shown in Figure 4G and I), the contrast-to-noise ratio estimated on the B-mode images for the two laterally central regions depicted in the original B-mode image shown in Figure 12A and B. The contrast-to-noise ratio is estimated on the B-mode images for the two laterally central regions depicted in the original B-mode image shown in Figure 12A and B: (**A**) using parabolic apodization for tr and re and (**B**) using non-parabolic apodization (ie, rectangular apodization) with non-steered spherical focusing for tr and re – ie, Focus(spx1,spx1).

Abbreviations: tr, transmission; re, reception; sp, spherical focusing using spherical waves; x1, non-crossed single wave; F(tr,re), spherical focusing for tr and re; A(tr,re), parabolic apodization for tr and re; and A(–), non-parabolic apodization using rectangular windows (ie, rectangular apodization or no apodization).

imaging and new LM displacement vector measurements. This meant (1) disregarding lateral low-frequency spectra (ie, filtering out lateral low-frequency spectra) and (2) the interchangeability of cosine and sine LMs. Specifically, disregarding lateral low-frequency spectra with cutoff frequencies ranging from 0 to 4.63 MHz (original LMs using crossed wave transmissions, ie, Methods A, B, D, and E), 0 to 3.46 MHz (original LMs with a non-steered single plane-wave transmission, ie, Methods C and F), and 0 to 2.29 MHz (quasi-LMs, ie, Methods G to J) resulted in a monotonic increase in all of the lateral frequencies from about 1.4 to 3.2 MHz up to about 3.6 to 5.4 MHz for the original LMs (Methods A to F),

from about 0.6 to 1.4 MHz up to about 2.4 to 3.6 MHz for the quasi-LMs (Methods G to J), and an increase in the axial frequencies, from about 6.9 to 7.2 MHz up to about 7.4 to 8.5 MHz for Methods A, B, D, and E, and from about 7.3 to 7.4 MHz up to about 8.1 to 8.6 MHz before decreasing (above approximately 1.5 MHz) for Methods C, F, and G to J (Figure 7). For the non-steered cases (Methods G to J), quasi-LMs were obtained (quasi-LMs generated the peaks of axial frequencies with smaller cutoff frequencies than the original LMs). Except for Method A, the cosine and sine LMs with proper cutoff frequencies were useful for LM echo imaging and LM displacement vector measurements, respectively. (With Method A, the cosine LM with a zero cutoff frequency was useful for both LM echo imaging and LM displacement vector measurement.[16]) All the new LMs were obtained after completing beamforming – that is, by post-processing of the generated beams or echo data. The incoherent superposition of divided spectra was also effective for speckle reduction.

As shown, the new SFDMs were particularly effective when rectangular apodization (for both transmission and reception) was used for crossed, steered spherical-focused beam transmission/reception scanning (Method D) and single spherical-focused beam transmission/reception scanning (Method I). The new SFDMs permitted the use of no apodization (ie, rectangular apodization) and/or simple non-steered single-beam scanning. For Methods D and I, the new SFDMs resulted in almost the same accuracy in measurements (eg, for displacement vectors, strain tensors, and shear moduli) that was obtained using the original LM method with parabolic apodization (Method A), as shown in Figures 10 and 11 (eg, for shear moduli measurements in the stiff inclusion, the relative means improved from 3.54 to 3.28 and from 3.59 to 3.27 vs 3.27; for SDs, from 0.37 to 0.34 and from 0.37 to 0.32 vs 0.33). Detection of the geometry of the stiff inclusion was also improved (ie, the circular shape became more accurate). Non-steered cases (eg, Method I) also require a smaller effective aperture size (8.8 mm) than the original LMs using crossed, steered beams – that is, conventional effective aperture sizes required to generate a single beam. This differs from the original LMs using a large effective aperture size and a deep region can be dealt with by using a small effective aperture size. For instance, such single-beam scanning can be effective for measurements of cardiac motion (eg, using a sector scan).

For comparison, single non-steered plane-wave transmissions (Methods C, F, H, and J) or crossed, steered plane-wave transmissions (Methods B and E) were also performed. For plane-wave transmissions, no apodization (ie, rectangular apodization) was performed, and for steered or non-steered spherical-focused beam transmissions/ receptions, rectangular or parabolic apodization was performed. Although the highest accuracy was not obtained using such beamforming methods, the new SFDMs produced an increase in measurement accuracy. In addition, the usefulness of plane-wave transmissions also increased – for example, for high-speed scanning of a target tissue with a rapid motion (such as blood flow in a carotid artery), the use of a 2D array-type transducer for 3D imaging/measurement and depth or axial compression/stretching strain measurement/ imaging. Specifically, for the respective original LM (Methods B, C, E, and F) and non-steered (Methods H and J) cases using plane waves, the parabolic (Methods B and C) and rectangular (Method J) apodizations were useful for beam reception. Although, for original LM, when such non-apodized, non-steered, or crossed plane waves are transmitted instead of spherical-focused beams, apodization for the reception of spherical-focused beams should be performed with Gaussian functions with long feet rather than parabolic functions with short feet, as shown in Sumi et al[15] and Sumi and Tanuma.[16] The Gaussian apodization was not performed in this report.

When raw spectra (Figures 4 and 5) were obtained using parabolic apodization (Methods A to C, G, and H) and no additional processing, the SNRs for the axial frequency range obtained with the original LM (Methods A to C) and non-steered (Methods G and H) cases were higher for the high axial frequency ranges than for the low axial frequency ranges. For the lateral frequency range, the SNRs obtained with the original LMs were almost same for the high and low lateral frequency ranges; the SNRs obtained for the non-steered cases were higher for the low lateral frequency ranges than for the high lateral frequency ranges. Alternatively, when using rectangular apodization (Methods D to F, I, and J), the SNRs obtained with the original LM (Methods D to F) and non-steered (Methods I and J) cases were higher for the low axial and lateral frequency ranges than for the high axial and lateral frequency ranges. Regarding the original LMs, for the axial direction, larger center frequencies and larger maximum frequencies for spectra were obtained with rectangular apodization than with parabolic apodization. Accordingly, because smaller lateral frequencies were obtained, steering with rectangular apodization should not be performed solo. That is, with no additional processing, large steering angles could not be obtained for US transmissions with crossed spherical beams, crossed plane waves, and a single non-steered plane wave. As shown, a lateral DC

and very low lateral frequency spectra were generated even with the original LMs (ie, Methods D to F using rectangular apodization). Accordingly, the corresponding echo images had no lateral oscillations.

Although the direction of propagation of US waves was controlled with higher accuracy when using plane-wave transmissions (single or crossed) than when using spherical-wave transmissions, low measurement accuracies and stabilities were obtained due to the low-echo SNRs obtained,[16] as shown in the agar phantom experiments. This was particularly noticeable for the original LM with rectangular apodization (Method E) rather than with parabolic apodization (Method B) (a much lower measurement accuracy and stability were obtained, although the difference of the obtained lateral frequencies was larger than with parabolic apodization – ie, for rectangular apodization for Methods D and E, 0.73 MHz; for parabolic apodization for Methods A and B, 0.20 MHz). In the original LMs, the non-steered single plane-wave transmissions yielded the lowest measurement accuracy of all,[16] although the higher measurement stability was obtained than the crossed, steered plane wave transmissions, particularly, with rectangular apodization (Figure 10E–H). Thus, for the original LMs, inherently, the combined use of rectangular apodization with plane-wave transmissions is not optimal. In the near future, results obtained using optimal Gaussian apodization[15,16] will be reported.

However, rectangular apodization yielded a larger lateral bandwidth than parabolic apodization for the original LM and non-steered cases. As shown for the use of rectangular apodization (in particular, Methods D and I), the effectiveness of disregarding low lateral frequency spectra was shown, even though high echo SNR components were disregarded. That is, monotonic increases in the lateral frequency were effectively obtained. As shown in Figure 7, due to the generation of slanted spectra (Figure 4), the axial frequencies also increased simultaneously (and, after reaching the maximum frequencies, the axial frequency decreased). Strictly speaking, due to the effects of increasing both the axial and lateral frequencies, measurement accuracies increased (Figures 10 and 11). In addition, quasi-LM echo imaging was also achieved for such non-steered cases (Figure 6G–J). Thus, reduced processing during beamforming (ie, no apodization and/or no generation of plural beams) also achieved a high measurement accuracy and LM echo imaging.

Specifically, for B-mode imaging using LMs, quasi-LMs, and other beamforming methods with parabolic and/or rectangular apodizations (Methods A to J), the superposition of coherent signals was detected with square detection (Figure 6). Although, in general, envelope detection, not square detection, is used for B-mode imaging, square detection was performed in this report to permit the visualization of wave oscillations (ie, to enable control by using the cutoff frequency f_c), which cannot be achieved using envelope detection. For all of the focusing methods, rectangular apodization also yielded higher axial spatial resolutions than parabolic apodization (ie, larger axial bandwidths). For sine and cosine LMs (Figures 6 and 7), for only very small cutoff frequencies, the differences in the generated lateral frequencies were notable, particularly for the non-steered cases and the original LMs with large lateral bandwidths (rectangular apodization) rather than for the original LMs with small lateral bandwidths (parabolic apodization). That is, sine LMs yielded higher LM frequencies than cosine LMs, particularly when a lateral narrow beam was generated – that is, when a large lateral bandwidth with a lateral DC and very low lateral frequency spectra were generated. The effects of disregarding low lateral frequency spectra were also confirmed visually in the B-mode images; although the lateral frequencies increased, the lateral spatial resolutions (lateral bandwidths) decreased. With respect to lateral spatial resolution, disregarding low lateral frequency spectra is counterproductive, except to visualize highly intense scattering waves or reflection waves (ie, speculars) originally obtained with a high spatial resolution (ie, rectangular apodization) through control of the cutoff frequency. Proper quasi-LM imaging can also be obtained similarly. Otherwise, disregard of low lateral frequency spectra is used for accurate measurements of displacement vectors and so forth. The effectiveness of incoherent superposition for B-mode imaging was also briefly mentioned with reference to figure 7 in Sumi et al.[15] For such incoherent superposition, the proper order of power for detection was also briefly mentioned, particularly for B-mode imaging and speckle reduction for a deep region.

The effects of disregarding low lateral frequency spectra were also evaluated using autocorrelation functions (Figures 8 and 9). As the generated lateral frequencies increased, the main lobes and side lobes became narrow and the number and magnitudes of side lobes increased. When using steered plane-wave transmissions or non-steered single plane-wave transmissions, large widths in the autocorrelation functions and large magnitudes in the side lobes were obtained. For the respective focusing methods, when using rectangular apodization, the widths of the autocorrelation functions were smaller than those obtained

using parabolic apodization. Moreover, the magnitudes of the side lobes obtained were smaller than those obtained using parabolic apodization. For all of the beamforming methods, due to a decrease in the ability to visualize the distribution of scattering properties with high spatial resolution, low frequencies or large magnitude side lobes decreased the accuracy of displacement measurements and the quality of B-mode imaging, except for permitting the visualization of intense scattering waves originally obtained with a high spatial resolution, as mentioned.

For Methods A to J, as shown in Figures 7, 10, and 11, accurate measurements of shear moduli were obtained using rather low cutoff frequencies (0 MHz or about 0.55 to 1.2 MHz). In particular, such low cutoff frequencies were used for the quasi-LM cases (about 0.15 to 0.5 MHz). As shown in Figure 9, although large lateral frequencies were also obtained with an optimal cutoff frequency (eg, for Method D, frequencies increased from 2.16 to 2.49 MHz; for Method I, from 1.44 to 1.67 MHz), large magnitude side lobes were not generated. Thus, evaluation of the autocorrelation function (PSF) can be used for determining a proper cutoff frequency.

However, as noted, with rectangular apodization, although Method E using crossed plane waves seemed to yield better autocorrelation functions with oscillations than Method D using crossed spherical waves, the measurement accuracies obtained were significantly lower (Figure 9). This was due to the low-echo SNR. As confirmed, the cutoff frequency was also sensitive to the measurement accuracy. Alternatively, Method I using non-steered beamforming yielded a low lateral frequency, although, with additional processing, the measurement accuracies became significantly high. This was due to a high echo SNR obtained in the high-frequency range as well as in the low-frequency range. For such beamforming, the evaluation of autocorrelation functions cannot be used to determine a proper cutoff frequency. For practical applications, such proper cutoff frequencies should be determined for the respective optional beamforming methods and US equipment in advance on the basis of the evaluation of actual measurement accuracies through phantom or other experiments (in vivo or in vitro experiments, etc) as performed in this report.

In this report, disregard of low-frequency spectra was performed in the lateral direction. As mentioned, such a SFDM is also effective for processing in the axial direction, that is, disregarding low axial frequency spectra (particularly when using parabolic apodization, ie, when low SNRs are obtained for lower axial frequency components).[53] This will be reported in detail elsewhere.

For speckle reduction, incoherent superposition (ie, square detection superposition) of horizontal, vertical, and simultaneous horizontal and vertical divisions of spectra was performed for beamforming Methods G and I (the corresponding spectra are shown in Figure 4G and I) with parabolic apodization for tr and re, and no apodization (rectangular apodization) with non-steered spherical focusing for tr and re. As shown for both apodizations, with the number of divisions increasing in the respective directions, the effects of speckle reduction were increased. Simultaneously, the spatial resolution decreased due to the decreases in the bandwidths. The effects of speckle reduction were the most pronounced for the simultaneous horizontal and vertical divisions. As a result, the existence of the inclusion was well visualized. The fine images were obtained with rectangular apodization rather than with parabolic apodization due to the inherent high spatial resolution. The difference can be confirmed for the remaining speckle sizes and the boundary between the inclusion and the surrounding region (particularly at the top and bottom boundaries due to the horizontal division). Moreover, the horizontal division was particularly effective with the intense scattering waves. The application of the new SFDMs using horizontal and vertical divisions will also be effective for physically steered cases, such as the original LMs and conventional steered beamforming. Speckle reduction was quantitatively evaluated using the SD/mean and the CNR was evaluated for log-scaled data because the images are shown in this scale. For the non-steering case, the new speckle reduction method using SFDMs is more effective with rectangular apodization than with parabolic apodization.

Conclusion
In summary, for physically steered beams with spherical focusing (LM cases) and quasi-steered beams (physically non-steered cases with spherical focusing), the new SFDMs were effective with the use of rectangular apodization because the originally visualized intense scattering waves with a high spatial resolution that were not well distinguished from surrounding scattering waves then became more clearly visualized using the lateral cutoff frequency (B-mode echo imaging). Further, a high degree of accuracy in the axial and lateral displacement measurements was achieved by generating high axial and lateral frequencies. That is, disregard of low lateral frequency spectra was effective when using cosine and sine LMs or quasi-LMs for the respective purposes. For imaging such specular waves, control of the low lateral cutoff frequency was effective. Also, for displacement vector measurements, the independence of the MAM simultaneous equations was increased. The simultaneous decrease in the axial and lateral bandwidths of such beams (ie, the broad-

ening of the beam width) was not sensitive with regard to measurement accuracy. It was possible, with the appropriate use of new SFDMs, for simple single-beam scanning or simple plural crossed-beam scanning with no apodization (ie, Methods I and D) to achieve almost the same accuracy as the original LM scanning method with parabolic apodization (Method A). In particular, the method will be effective (eg, for tissue elasticity measurements/imaging using low-frequency tissue deformation and measuring blood flow) when the spatial frequency of a target displacement distribution is low (ie, the distribution is continuous or smooth). However, an excessive disregard of low-frequency spectra can lead to a decrease of echo SNRs as well as axial bandwidths and the accuracy of a displacement vector measurement. Moreover, for the original LMs using crossed, steered plane transmissions and non-steered single plane-wave transmissions for rapid scanning, rectangular apodization did not yield accurate measurements, although measurement accuracy was increased by disregarding spectra. For instance, for plane-wave transmissions, Gaussian apodization is appropriate.[15,16] However, appropriate or optimal functions must still be examined for particular beamforming methods (eg, ASTA with a non-zero steering angle; LM with non-symmetrically steered beams, sector, arc, and radial scanning), as well as for the geometry of the transducer apertures (linear, convex types, etc), and an optimization method previously described[47–49] can be used. In the Methods section, other methods appropriate for disregarding spectra are described (eg, for ASTA with a non-zero steering angle, rotation of coordinate system for ASTA or LM etc). In future, windows for dividing spectra with weights[53] will also be used to increase the accuracy and stability in a measurement.

Although in this report B-mode imaging of LMs and quasi-LMs was performed through square detection of coherently superposed echo signals (beams or quasi-beams), as mentioned, speculars such as intense scattering waves and reflection waves can be more clearly visualized using incoherent superposition, as previously shown in Sumi et al[15] (and not coherent superposition). Such imaging can also be performed with a low lateral cutoff frequency and this will be reported in detail elsewhere. The order of power (detection) to be superposed will also be reported in detail elsewhere (also for speckle reduction). Regarding the visualization of wave oscillations, a comparison with envelope detection will also be reported, along with the disregard of low axial frequency spectra.

In this report, the use of square rather than envelope detection was focused on, for the new speckle reduction method. Speckle reduction using the new SFDMs

with incoherent superposition was performed only for non-steered single-beam scanning, and its effectiveness was confirmed. For non-steered single-beam scanning, only horizontal division, only vertical division, or both horizontal and vertical divisions were performed independently or simultaneously. Results obtained using both horizontal and vertical divisions performed independently (not shown) will be reported elsewhere.[54] The lines and planes can be slanted or curved, but this was not considered in this study. The use of the envelope detection will be reported in detail elsewhere, together with speckle reduction using the original LM method with plural physically generated beams and other arbitrary beamforming methods, such as conventional beamforming and ASTA.[37,50,51,54] Similarly to the non-steered single-beam scanning, a large number of physically generated beams and/or quasi-beams with various different steering angles will be used.

In conjunction with the new SFDMs, over-determined systems can be obtained for measuring a displacement vector.[35,37,50,51,53–56] Basically, SFDMs are used on coherent beams that are generated to obtain new quasi-beams with different beam properties, such as US frequencies, steering angles (lateral frequencies), bandwidths, and F-numbers.[35–37,50,51] Such over-determined systems can also be obtained from the use of plural physically generated beams, of which the number is larger than that required for the original LM method (ie, two for a 2D displacement vector measurement and three for a 3D displacement vector measurement). Further, for a single steered or non-steered beam, a much larger number of quasi-beams than that required for the original LM method (an overdetermined system) can also be obtained. The SFDMs can also be used with plural beams. Because a larger number of simultaneous equations (MAM or MDM[13] and SFDM[23]) are derived, the least squares method can be used to solve the equations. Alternatively, the measurements obtained using a single equation (ie, an equation for 1D AM or 1D DM) or partial simultaneous equations can also be superposed to obtain the final measurement result. The equations or measurement results obtained from the respective beams or quasi-beams are weighted by the confidence of the beams or quasi-beams evaluated by Ziv-Zakai lower bound or energy.[35,37,50,51,53–56] The confidence can also be determined using the variance of the measurement results a posteriori. Such weighting can also be performed at the respective measurement positions eg.[10,11,57–60] When an overly large number of divisions yields low SNR coherent signals, measurement accuracy decreases. For instance, a high measurement accuracy was obtained for both the horizontal and vertical divisions when performed independently and

yielded more accurate measurements of axial displacement/strain (ie, axial compression or stretching) than if both divisions were performed simultaneously.[35,55,56] For other methods of generating such new beam properties, a coherent superposition of various beams can also be performed (eg, non-focused, steered, or non-steered plane waves).[37,50–52] The SFDMs can also be used on such a generated beam. B-mode imaging and speckle reduction can be performed together.

For 3D echo imaging, 3D displacement vector measurements, and 3D speckle reduction, the corresponding three new SFDMs are described in Appendix A (ie, applications to lateral and elevational modulations or their quasi-modulations using horizontal and/or vertical planes such as flat, curved or slanted ones). For the 3D cases, experimental data will be presented elsewhere.

Disclosure
The authors report no conflicts of interest in this work.

References
1. Satomura S. Study of the flow patterns in peripheral arteries by ultrasonics. *J Acoust Soc Jpn*. 1959;15:151–158.
2. Baker DW. Pulsed ultrasonic Doppler blood-flow sensing. *IEEE Trans Sonics Ultrason*. 1970;17(3):170–185.
3. Kasai C, Namekawa K, Koyano A, Omoto R. Real-time two-dimensional blood flow imaging using an autocorrelation technique. *IEEE Trans Sonics Ultrason*. 1985;32(3):458–464.
4. Foster SG, Embree PM, O'Brien WD. Flow velocity profile via time-domain correlation: error analysis and computer simulation. *IEEE Trans Ultrason Ferroelectr Freq Control*. 1990;37(3):164–175.
5. Wilson LS, Robinson DE. Ultrasonic measurement of small displacements and deformations of tissue. *Ultrason Imaging*. 1982;4(1):71–82.
6. Ophir J, Céspedes I, Ponnekanti H, Yazdi Y, Li X. Elastography: a quantitative method for measuring the elasticity of biological tissues. *Ultrason Imaging*. 1991;13(2):111–134.
7. Trahey GE, Allison JW, von Ramm OT. Angle independent ultrasonic detection of blood flow. *IEEE Trans Biomed Eng*. 1987;34(12): 965–967.
8. Yagi S, Nakayama K. Local displacement analysis of inhomogeneous soft tissue by spatial correlation of rf echo signals. *Proceedings of World Federation of Ultrasound in Medicine and Biology*; Oct 1988; Washington DC. p. 113.
9. Sumi C, Suzuki A, Nakayama K. Phantom experiment on estimation of shear modulus distribution in soft tissue from ultrasonic measurement of displacement vector field. *IEICE Trans Fundamental*. 1995;E78-A(12): 1655–1664.
10. Sumi C. Fine elasticity imaging on utilizing the iterative RF-echo phase matching method. *IEEE Trans Ultrason Ferroelectr Freq Control*. 1999;46(1):158–166.
11. Sumi C. Digital measurement method of tissue displacement vector rrom instantaneous phase of ultrasonic echo signal. Technical report. Tokyo: Japan Society of Ultrasound Medicine; 2002:37–40.
12. Sumi C. Multidimensional displacement vector measurement methods utilizing instantaneous phase. *Conf Proc IEEE Eng Med Biol Soc*. 2005;2:1704–1707.
13. Sumi C. Displacement vector measurement using instantaneous ultrasound signal phase -multidimensional autocorrelation and doppler methods. *IEEE Trans Ultrason Ferroelectr Freq Control*. 2008; 55(1):24–43.
14. Sumi C. Improvement of measurement accuracy of displacement vector by lateral modulation. *Proceedings of the 2004 Autumn Meeting Acoustical Society of Japan*; 2004 Sep; Okinawa, Japan. pp. 1353–1354. Japanese.
15. Sumi C, Noro T, Tanuma A. Effective lateral modulations with applications to shear modulus reconstruction using displacement vector measurement. *IEEE Trans Ultrason Ferroelectr Freq Control*. 2008;55(12):2607–2625.
16. Sumi C, Tanuma A. Comparison of parabolic and Gaussian lateral cosine modulations in ultrasound imaging, displacement vector measurement, and elasticity measurement. *Jpn J Appl Phys*. 2008;47(5):4137–4144.
17. Sumi C, Matsui N, Shimizu K, Takanashi Y. Preliminary experiments on virtual source for lateral modulation. *Proceedings of the 8th International Conference on the Ultrasonic Measurement and Imaging of Tissue Elasticity*; September 14–17, 2009; Vlissingen, The Netherlands. Available from: http://www.elasticityconference.org/prior_conf/2009/PDF/088SumiC02FP.pdf. Accessed July 11, 2012.
18. Sumi C. Utilization of an ultrasound beam steering angle for measurements of tissue displacement vector and lateral displacement. *Reports in Medical Imaging*. 2010;3:61–81.
19. Sumi C, Shimizu K. Ultrasonic agar phantom experiment for comparison of the measurement accuracy of tissue elasticity obtained by displacement vector measurement using lateral modulation with multidimensional autocorrelation and Doppler methods and corresponding one-dimensional methods. *Reports in Medical Imaging*. 2011;4:39–46.
20. Sumi C. Usefulness of ultrasonic strain measurement-based shear modulus reconstruction for diagnosis and thermal treatment. *IEEE Trans Ultrason Ferroelectr Freq Control*. 2005;52(10):1670–1689.
21. Sumi C. Relative shear modulus reconstruction for visualization with no geometrical artifact. *Acousl Sci Technol*. 2010;31(5):347–359.
22. Sumi C, inventor. Displacement measurement method and apparatus, strain measurement method and apparatus, elasticity and viscoelasticity constants measurement apparatus, and the elasticity and viscoelasticity constants measurement apparatus based treatment apparatus. Japanese patent 4260523. April 30, 2009. United States patent US 7775980 B2. August 17, 2010. Available from: http://www.google.com/patents/US7775980.pdf. Accessed July 11, 2012.
23. Sumi C, Ichimaru K, Shinozuka Y. Beam steering and coordinate system rotation improves accuracy of ultrasonic measurements of tissue displacement vector and lateral displacement. *Reports in Medical Imaging*. 2011;4:47–66.
24. Jensen JA, Munk P. A new method for estimation of velocity vectors. *IEEE Trans Ultrason Ferroelectr Freq Control*. 1998;45(3): 837–851.
25. Jensen JA. A new estimator for vector velocity estimation. *IEEE Trans Ultrason Ferroelectr Freq Control*. 2001;48(4):886–894.
26. Aderson ME. Multi-dimensional velocity estimation with ultrasound using spatial quadrature. *IEEE Trans Ultrason Ferroelectr Freq Control*. 1998;45(3):852–861.
27. Anderson ME. A heterodyning demodulation technique for spatial quadrature. *2000 IEEE Ultrasonics Symposium: Proceedings*. 2000;2(2):1487–1490.
28. Fox MD. Multiple crossed-beam ultrasound Doppler velocimetry. *IEEE Trans Ultrason Ferroelectr Freq Control*. 1978;25(5):281–286.
29. Azar RZ, Baghani A, Salcudean SE, Rohling R. 2-D high-frame-rate dynamic elastography using delay compensated and angularly compounded motion vectors: preliminary results. *IEEE Trans Ultrason Ferroelectr Freq Control*. 2010;57(11):2421–2436.
30. Tanter M, Bercoff J, Sandrin L, Fink M. Ultrafast compound imaging for 2-D motion vector estimation: application to transient elastography. *IEEE Trans Ultrason Ferroelectr Freq Control*. 2002;49(10): 1363–1374.
31. Sumi C, Ebisawa T. Phantom experiments of axial strain measurements using multidimensional autocorrelation method, multidimensional Doppler method and direct strain measurement method. *Acoust Sci Technol*. 2009;30(2):124–131.

32. Sumi C. Ultrasonic measurement and imaging with lateral modulation – echo, tissue motion and elasticity. In: Tanabe M, editor. *Ultrasound Imaging*. Rijeka: InTech; 2011:113–138. Available from: http://www.intechopen.com/books/ultrasound-imaging/ultrasonic-measurement-and-imaging-with-lateral-modulation-echo-tissue-motion-and-elasticity. Accessed July 11, 2012.

33. Sumi C, Takanashi Y, Ichimaru K. Consideration of generated beam angles increases the accuracy of ultrasonic displacement measurements. *Reports in Medical Imaging*. 2012;5:23–50.

34. Sumi C. Multidimensional ultrasonic imaging and displacement vector measurement using spectra frequency division method. *IEICE Technical Report*. 2011;US-07:85–90. Japanese.

35. Sumi C, Takahashi Y, Ishii Y, Yamazaki N. A lateral modulation imaging using simple nonsteering beamforming. In: Abstract of the *10th International Conference on the Ultrasonic Measurement and Imaging of Tissue Elasticity;* October 12–15, 2011; Arlington, TX: 73. Abstract published October 12, 2011. Available from: http://www.elasticityconference.org/prior_conf/2011/PDF/2011ITECProceedings.pdf. Also in: *Proceedings of The International Tissue Elasticity Conference*. Available from: http://www.elasticityconference.org/prior_conf/2011/PDF/064SumiC02FP.pdf. Accessed January 23, 2011.

36. Sumi C. New echo imaging and displacement measurement using steering beams. *Japanese Journal of Medical Ultrasonics*. 2011;38(Suppl):S260. Abstract of the 84th Annual Scientific Meeting of the Japan Society of Ultrasonics in Medicine; May 2011; Tokyo, Japan. Published April 15, 2011.

37. Sumi C, inventor; assignee. Clinical apparatuses. United States patent US8211019B2. July 3, 2012.

38. Carpenter DA, Dadd MJ, Kossoff G. A multi-mode real-time scanner. *Ultrasound Med Biol*. 1980;6(3):279–284.

39. Berson M, Roncin A, Pourcelot L. Compound scanning with an electrically steered beam. *Ultrason Imaging.* 1981;3(3):303–308.

40. Shattuck DP, von Ramm OT. Compound scanning with a phased array. *Ultrason Imaging.* 1982;4(2):93–107.

41. Jespersen SK, Wilhjelm JE, Sillesen H. Multi-angle compound imaging. *Ultrason Imaging.* 1998;20(2):81–102.

42. Entrekin RR, Porter BA, Sillesen HH, Wong AD, Cooperberg PL, Fix CH. Real-time spatial compounding imaging: application to breast, vascular, and musculoskeletal ultrasound. *Semin Ultrasound CT MR*. 2001;22(1):50–64.

43. Trahey GE, Smith SW, von Ramm OT. Speckle pattern correlation with lateral aperture translation: experimental results and implications for spatial compounding. *IEEE Trans Ultrason Ferroelectr Freq Control*. 1986;33(3):257–264.

44. Magnin PA, von Ramm OT, Thurstone FL. Frequency compounding for speckle contrast reduction in phased array images. *Ultrason Imaging.* 1982;4(3):267–281.

45. Melton HE Jr, Magnin PA. A-mode speckle with compound frequencies and compound bandwidths. *Ultrason Imaging.* 1984;6(2):159–173.

46. Trahey GE, Allison JW, Smith SW, von Ramm OT. A quantitative approach to speckle reduction via frequency compounding. *Ultrason Imaging.* 1986;8(3):151–164.

47. Sumi C, Shimizu K, Takanashi Y, Tadokoro Y, Nozaki Y. 2nd report on proper point spread function for lateral modulation. *Proceedings of the 8th International Conference on the Ultrasonic Measurement and Imaging of Tissue Elasticity*; September 14–17, 2009; Vlissingen, The Netherlands. 2010. Available from: http://www.elasticityconference.org/prior_conf/2009/PDF/087SumiC01FP.pdf. Accessed July 11, 2012.

48. Sumi C, Shimizu K, Matsui N. Proper analytic point spread function for lateral modulation. *Jpn J Appl Phys*. 2010;49(7B):07HF07.

49. Sumi C, Komiya Y, Uga S. A demonstration of optimal apodization determination for proper lateral modulation. *Jpn J Appl Phys*. 2009; 48(7B):07GJ06.

50. Sumi C, inventor. Displacement measurement method and ultrasonic apparatus. Japanese patent 4731863. April 28, 2011.

51. Sumi C, inventor. Displacement and strain measurement method and apparatus, strain measurement method, elasticity and viscoelasticity measurement apparatus, ultrasonic diagnosis apparatus. Japanese patent publication JP-P2007-152074A. June 21, 2007.

52. Sumi C, Ishii Y, Hirabayashi Y. Increase in accuracy of tissue displacement vector measurement and speckle reduction using coherent and incoherent superposition of multidimensional echo signals. *IEICE Technical Report*. 2012;112(16):33–38. Japanese.

53. Sumi C, Ishii Y. Tissue ultrasound imaging and displacement measurement using weighting of echo spectra and over-determined system - Included cases using high intensity ultrasound for thermal treatment and radiation force. *IEICE Technical Report*. 2012;US-9:7pp. In press.

54. Sumi C, Ishii Y, Yamazaki N, Hirabayashi Y. Applications of coherences of ultrasounds and low frequency waves. In: Abstracts of the *11th International Conference on the Ultrasonic Measurement and Imaging of Tissue Elasticity*; October 2–5, 2012; Deauville, France. In press. Also in: *Proceedings of the International Tissue Elasticity Conference*. In press.

55. Sumi C, Takanashi Y, Ichimaru K. Accuracy of measurements of tissue lateral displacement and displacement vector using laterally wide wave transmission for high speed scanning over region of interest. *IEICE Technical Report*. 2011;US-10:23–28.

56. Sumi C, Ishii Y, Yamazaki N. Ultrasonic tissue displacement measurement and speckle reduction using plural beams or spectra frequency division method. *Transactions of the Japanese Society for Medical and Biological Engineering*. 2012;50(Suppl):About 2 pp.

57. Sumi C. Regularization for ultrasonic measurements of tissue displacement vector and strain tensor. *IEEE Trans Ultrason Ferroelectr Freq Control*. 2008;55(4):787–799.

58. Sumi C. Regularization of tissue shear modulus reconstruction using strain variance. *IEEE Trans Ultrason Ferroelectr Freq Control*. 2008; 55(2):297–307.

59. Sumi C, Itoh T. A limitation in the use spatially stationary strain variance estimation in the regularization of shear modulus reconstruction. *Acoust Sci Tech*. 2010;31(5):360–367.

60. Sumi C, Itoh T. Spatially variant regularization of lateral displacement measurement using variance. *Ultrasonics*. 2009;49:459–465.

Appendix
SFDMs for 3D measurement/imaging and speckle reduction

For 3D spectra, horizontal or vertical planes can be used. Similarly to the case for 2D, a number of vertical or horizontal planes can also be used. The planes can be slanted or curved.

Figure A1 shows schematics for 3D imaging/measurement using non-steered single-beam scanning: (A1A) apodization function (ie, a symmetric two-dimensional function with a peak); (A1B) lateral and elevational cosine modulations achieved after performing such beamforming by filtering out lateral and elevational low-frequency spectra in a frequency domain; (A1C) interchangeability of cosine and sine modulations about lateral and elevational modulations with almost the same modulation frequencies – that is, by changing the sign of the spectra of either positive or negative lateral and elevational frequencies; (A1D) lateral and elevational sine modulations achieved using asymmetric apodization, even without lateral and elevational low-frequency filtering shown in A1B. Moreover, for the lateral and elevational sine

modulations shown in Figure A1D, the disregard of low-frequency spectra shown in Figure A1B can be implemented for controlling the lateral and elevational modulation frequencies. The corresponding processing for 2D imaging/measurement is shown in Figure 1. When performing steered beamforming, similar to the 2D case shown in the left top panel of Figure 1C, such processing can be performed.

Figure A2 shows schematics for 3D imaging/measurement using the original modulation method with physically crossed, steered beams: (A2A) apodization function (ie, a symmetric 2D function with four peaks and, although not shown, three peaks can also be used instead) for lateral and elevational cosine modulations; (A2B) processing for increasing lateral and elevational modulation frequencies after performing such beamforming – that is, by filtering out lateral and elevation low-frequency spectra in a frequency domain; (A2C) interchangeability of cosine and sine modulations about lateral and elevational modulations – that is, by changing signs of the spectra of either positive or negative lateral and elevational frequencies; (A2D) lateral and elevational sine modulations achieved using laterally and
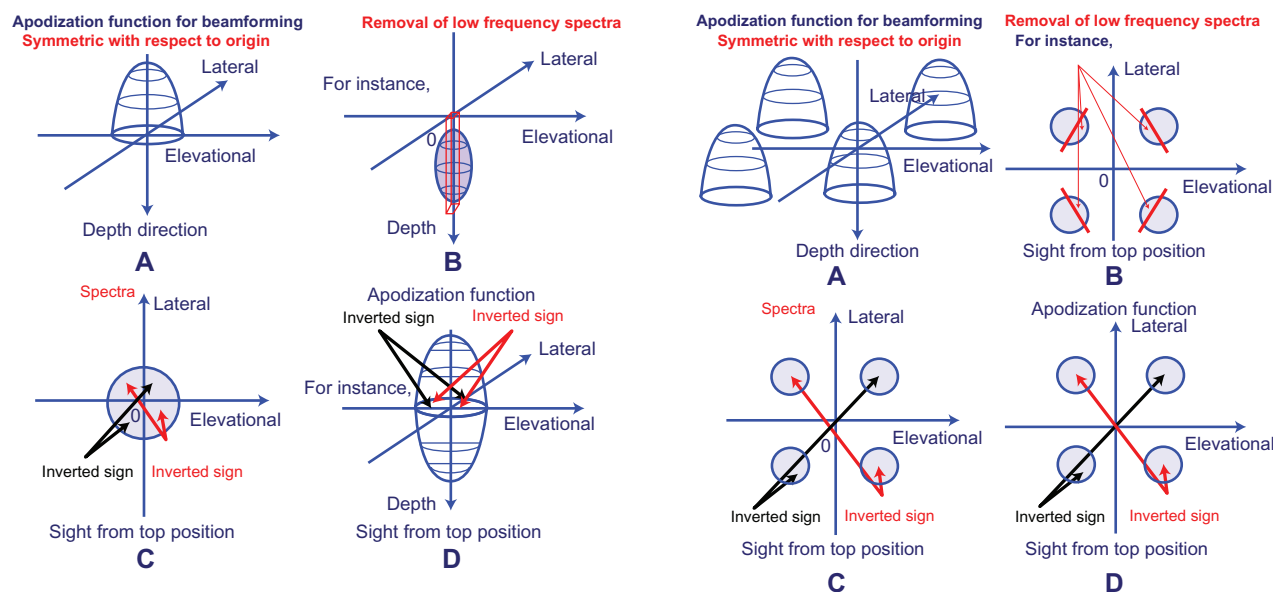

Figure A1 Schematics for three-dimensional imaging/measurement using non-steered single-beam scanning: (**A**) apodization function (ie, a two-dimensional function with a peak symmetric in the lateral and elevational directions); (**B**) lateral and elevational cosine modulations achieved after performing such beamforming (ie, by filtering out lateral and elevational low-frequency spectra in a frequency domain); (**C**) interchangeability of cosine and sine modulations about lateral and elevational modulations achievable (ie, by changing the sign of the spectra of either the positive or negative lateral and elevational frequencies); (**D**) lateral and elevational sine modulations can also be achieved by using asymmetric apodization, even without the lateral and elevational low-frequency filtering shown in **B**. Also, for the lateral and elevational sine modulations shown in **D**, disregard of low-frequency spectra shown in **B** can be implemented for controlling the lateral and elevational modulation frequencies. The processing may also be performed on a steering beam and the apodization function is not always symmetric (not shown).

Figure A2 Schematics for three-dimensional imaging/measurement using the original lateral modulation method with physically crossed, steered beams: (**A**) apodization function (ie, a symmetric two-dimensional function with four peaks and three peaks [not shown] can also be used instead) for lateral and elevational cosine modulations; (**B**) processing for increasing the lateral and elevational modulation frequencies after such beamforming (ie, by filtering lateral and elevational low-frequency spectra in a frequency domain); (**C**) interchangeability of cosine and sine modulations about lateral and elevational modulations (ie, by changing the sign of the spectra of either the positive or negative lateral and elevational frequencies); (**D**) lateral and elevational sine modulation can also be achieved by using laterally and elevationally asymmetric apodization. Such an apodization symmetric with respect to the depth axis is not always performed, and the directions of modulations may also be slanted (not shown).

elevationally asymmetric apodization. Further, for the lateral and elevational sine modulations shown in Figure A2D, the disregard of low-frequency spectra shown in A2B can be implemented for controlling the lateral and elevational modulation frequencies. The corresponding processing for 2D imaging/measurement is shown in Figure 2.

For 3D echo imaging, 3D displacement vector measurement, and 3D speckle reduction, such obtained echo data can be used in a manner similar to those of 2D cases. When obstacles such as bones exist, the crossed beams

or quasi-beams may also be generated non-symmetrically with respect to the depth axis (not shown in Figures A1 and A2).[17,18,23] A proper apodization function may also be determined using an optimization method previously developed,[47–49] although apodization functions can also be designed by simply using a coordinate rotation of analytical apodization functions. The coordinate system may also be rotated.[17,18,23] In future studies, for the spectra division, flat, curved, or slanted horizontal and/or vertical planes will be used. Experimental data will be presented elsewhere.